universität wien

MASTERARBEIT / MASTER'S THESIS

Titel der Masterarbeit / Title of the Master's Thesis

„Post-Genomic Investigations of Cell Death Mechanisms“

verfasst von / submitted by

Nina Hochmeister, BSc

angestrebter akademischer Grad / in partial fulfilment of the requirements for the degree of

Master of Science (MSc)

Wien, 2023 / Vienna 2023

Studienkennzahl lt. Studienblatt / degree programme code as it appears on the student record sheet:	A 066 862
Studienrichtung lt. Studienblatt / degree programme as it appears on the student record sheet:	Masterstudium Chemie
Betreut von / Supervisor:	Ass.-Prof. Dr. Samuel Matthias Meier-Menches

Acknowledgements

First and foremost, I would like to express my gratitude to my supervisor Ass.-Prof. Dr. Samuel Meier-Menches for giving me the opportunity to work with him and his group on such an exciting project, for his professional assistance and for his encouragement in challenging situations.

Furthermore, I would like to pay my special regards to Univ.-Prof. Dr. Christopher Gerner and Dr. Michael Jakupec and their research groups for their warm welcome and contributions. My sincere thanks go especially to my co-supervisor Yasmin Borutzki, who supported me throughout my work and shared her invaluable advice and experience with me. I would like to thank Klaudia Cseh and Lukas Skos for introducing me to cell culture techniques and always supporting me during the experiments. Thanks to them, I discovered my passion for cell culture experiments. Special thanks go to Gerhard Hagn and Dr. Thomas Mohr, as they helped me a lot with the statistical analysis. Furthermore, I am very grateful to Patricia Bortel, who introduced me to the world of phosphoproteomics and to Dr. Andrea Bileck for proteomic data acquisition.

I would also like to thank Benjamin Zourek for his creative support.

Lastly, I want to thank my family who have been continuously supportive and encouraging on my educational journey.

Zusammenfassung

Apoptose ist ein wichtiger Zelltodmechanismus in der Krebstherapie. Einige Krebsarten sind jedoch von Natur aus resistent gegen diese Behandlung, vor allem Krebs mesenchymalen Ursprungs. Kürzlich wurde festgestellt, dass diese Krebsarten empfindlich auf Ferroptose reagieren, eine alternative Form des Zelltods, deren Mechanismus jedoch noch nicht vollständig geklärt ist. In dieser Arbeit wurden die Mechanismen von Apoptose und Ferroptose auf molekularer Ebene mit Hilfe von biochemischen Assays und Omics-Techniken in der Ovarialkarzinomzelllinie A2780 charakterisiert und verglichen. Apoptose und Ferroptose wurden jeweils mit Cisplatin- und RSL-3-Behandlungen chemisch induziert. Vorherige Experimente zur Bewertung der Caspase-Aktivität auf Proteomebene haben gezeigt, dass die A2780-Zelllinie ein geeignetes Modell zur Untersuchung dieser Zelltodwege ist. Dabei wurde festgestellt, dass der Caspase-3-Inhibitor Z-DEVD-FMK die Zytotoxizität von Cisplatin spezifisch reduziert, während der Ferroptose-Inhibitor Ferrostatin-1 die RSL-3-Zytotoxizität vollständig hemmt. Ein durchflusszytometrischer Annexin-V/Propidiumiodid-Test offenbarte einen signifikanten Anteil von Zellen mit freiliegendem Phosphatidylserin auf der äußeren Membran, zusammen mit permeabilisierten Membranen für beide Typen. Die Ferroptose zeichnete sich durch eine minimale Zellpopulation aus, die zwar eine Freisetzung von Phosphatidylserin, aber keine Membranpermeabilisierung aufwies, während bei der durch Cisplatin induzierten Apoptose ein signifikanter Anteil dieser Zellen zu finden war. Interessanterweise ergab der DCFH-DA-Test, dass weder bei Apoptose noch bei Ferroptose vermehrt lösliche reaktive Sauerstoffspezien (ROS) vorhanden waren. Darüber hinaus ergab eine nicht zielgerichtete Metabolomik-Analyse der Überstände nur geringe Veränderungen bis zu 24 Stunden nach der Induktion des Zelltods. Von den 82 Metaboliten wurde Epinephrin als Stressmarker in beiden Fällen hochreguliert gefunden. Außerdem war das fehlende Ausscheiden von 4-Aminobenzoesäure aus Cisplatin-behandelten Zellen in den Überstand ein auffälliges Merkmal der Apoptose. Die Phosphoproteomanalyse ganzer Zelllysate nach 4-stündiger Behandlung ergab >4500 Phosphopeptide und eine verringerte Aktivität der Tyrosinkinasen, mit Ausnahme der *Src*-Kinase.

Folglich bietet diese Studie einen detaillierten Einblick in die molekularen Mechanismen von Apoptose und Ferroptose, der in die phänotypische Arzneimittelforschung einfließen könnte, um Ferroptose-induzierende Wirkstoffe mithilfe von biochemischen Analysen und Omics-Signaturen zu identifizieren.

Abstract

Apoptosis represents an important cell death mechanism for anticancer therapy. However, several cancer types are intrinsically resistant to this treatment, mainly cancer of mesenchymal origin. It was recently revealed that those cancer types are vulnerable to ferroptosis, which is an alternative form of cell death, but whose mechanism is not yet fully elucidated. This thesis set out to characterise and contrast apoptosis and ferroptosis mechanisms on the molecular level using biochemical assays and omics techniques in the A2780 ovarian cancer cell line. Apoptosis and ferroptosis were chemically induced with cisplatin (CisPt) and RSL-3 treatment, respectively. Preliminary experiments that evaluated caspase activity on the proteome level have shown that the A2780 cell line is a suitable model to investigate these cell death pathways. In the frame of this thesis, it was found that the caspase-3 inhibitor Z-DEVD-FMK reduced specifically the cytotoxicity of CisPt, while the ferroptosis inhibitor ferrostatin-1 completely inhibited RSL-3 cytotoxicity. A flow cytometric annexin-V/propidium iodide assay revealed a significant proportion of cells with exposed phosphatidylserine (PS) on the outer membrane, together with permeabilized membranes for both types. Ferroptosis was characterized by a minimal cell population displaying PS exposure and no membrane permeabilization, while apoptosis induced by CisPt featured a significant fraction of those. Interestingly, neither apoptosis nor ferroptosis were characterized by increased soluble reactive oxygen species (ROS) as revealed by the DCFH-DA assay. Furthermore, a non-targeted metabolomics assay of the supernatants revealed only minor changes up to 24 h of cell death induction. Of the 82 confidently identified metabolites, epinephrine as a stress marker was found upregulated in both cases. Moreover, the lack of 4-aminobenzoic acid export from CisPt-treated cells into the supernatant was a striking feature of apoptosis. Phosphoproteomic analysis of whole cell lysates after 4 h treatment revealed >4500 phosphopeptides and subsequent kinase substrate enrichment analysis indicated a reduced activity of tyrosine kinases in general, except for *Src* kinase.

Consequently, this study provides detailed insight into the molecular mechanisms of apoptosis and ferroptosis, which might be implemented into phenotypic drug discovery to identify ferroptosis-inducing agents specifically based on molecular signatures.

Table of contents

Abbreviations

2-CAM	2-cloroacetamide
AA	antimycin A
ACN	acetonitrile
ATP	adenosine triphosphate
AUC	areas under the curve
AV	annexin-V
BB	binding buffer
BCA	bicinchoninic acid
BID	BH3 interacting domain death agonist
BSA	bovine serum albumin
CisPt	cisplatin
DCF	2`,7`-dichlorofluorescein
DCFH	2`,7`-dichlorodihydrofluorescein
DCFH-DA	dichloro-dihydro-fluorescein diacetate
ECAR	extracellular acidification rate
EP	EasyPhos
ESI	electrospray ionization
FA	formic acid
FBS	fetal bovine serum
FC	fold change
FDR	false discovery rate
glyco	glycolytic
GPX4	glutathione peroxidase 4
GSH	glutathione
HCD	higher-energy collisional dissociation
HILIC	hydrophilic interaction liquid chromatography
IC_{50}	half maximal inhibitory concentration
IMMS	ion mobility mass spectrometry
IST	internal standard
KSEA	kinase-substrate enrichment analysis
LC	liquid chromatography
LFQ	label free quantification
m/z	mass-to-charge-ratio
MeOH	methanol
mito	mitochondrial
MS	mass spectrometry
MTT	3-(4,5-dimethylthiazol-2-yl)-2,5-diphenyltetrazolium bromide
OCR	oxygen consumption rate
OM	oligomycin
PABA	4-aminobenzoic acid
PBS	phosphate buffered saline
PCA	principal component analysis
PI	propidium iodide
PTM	post translational modification

PUFA	polyunsaturated fatty acids
Q	quadrupole
QQQ	triple quadrupole
R	rotenone
RCD	regulated cell death
ROS	reactive oxygen species
RP	reversed-phase
SDB-RPS	styrenedivinylbenzene-reverse phase sulfonate
SDC	sodium deoxycholate detergent
T25	25 cm^2 culture flasks
T75	75 cm^2 culture flasks
TBHP	tert-Butyl hydroperoxide
TBS	tris-buffered saline
TCEP	tris(2-carboxyethyl)phosphine
TFA	trifluoroacetic acid
TIMS	trapped ion mobility spectrometry
TK	tyrosine kinases
TOF	time-of-flight
UHPLC	ultra high-performance liquid chromatography

1 Introduction

Cell death plays a crucial role for regular development, homeostasis, and the prevention of hyperproliferative diseases like cancer. Historically, due to morphological observations cell death has been divided into apoptosis (programmed cell death), and necrosis (accidental cell death). Traditionally, it was taught that in mammalian cells almost all regulated cell death (RCD) resulted from apoptosis. But the discovery of various regulated non-apoptotic cell death mechanisms refuted this statement. Nowadays, there are more alternative cell death pathways renowned such as autophagy, necrotic apoptosis, or ferroptosis. (1–4)

Anticancer chemotherapy relies crucially on the induction of cell death as the main tumour-inhibiting process. Cisplatin (CisPt), and its derivates, carboplatin and oxaliplatin, are one of the most widely used chemotherapeutic anticancer drugs in clinical use. Both CisPt and carboplatin cause DNA damage, while oxaliplatin stresses ribosomal biogenesis, with all three drugs leading to the induction of the apoptotic pathway. Nevertheless, there are some drawbacks with these platinum-based drugs such as the problem of inherent or therapy-induced resistance of cancer cells. Hence, the exploration of alternative RCD pathways plays an important role for finding cancer treatments with enhanced efficacy. Ferroptosis may represent a promising alternative cell death mechanism. It is completely independent from apoptosis and cells, which are classically resistant to apoptosis-inducing agents, are often vulnerable to ferroptosis induction. Interestingly, cells cannot be resistant to apoptosis and ferroptosis at the same time. An increased understanding for both processes is needed for the development of efficient therapeutic interventions. (5–11)

1.1 Carcinogenesis

Normally, cell proliferation and cell death are naturally in balance. In contrast, cancer is the result of accumulation of gene mutations which gradually increase cell proliferation. The mutations can be caused by environmental factors, inheritance, or DNA replication errors. Overall, approximately three mutations occur every time during cell division of a normal human stem cell. However, cancer can appear in every cell of the body, thus

around 200 different kinds of cancer and over 1.000 various subgroups are known. (12, 13)

Lately, there are eight hallmarks of cancer which propose capabilities for the formation of malignant tumours: resisting cell death, reprogramming cellular metabolism, evading growth suppressors, avoiding immune destruction, activating invasion and metastasis, sustaining proliferative signalling, enabling replicative immortality, and inducing/accessing vasculature. Moreover, there is a great variety of the underlying mechanisms of the eight capabilities. (14, 15)

Although, tumours are heterogenous and diverse, there is one thing they all have in common: the ability to perform cell proliferation beyond the limits of normal cell growth. In almost any event, neoplastic progression is the result of supressed cell death and dysfunctional cell proliferation. The big challenge is to identify the differences between tumour cells and normal ones and to explore how these varieties can be used for therapy design. (16, 17)

1.2 Apoptosis

Apoptosis is a controlled, energy-driven cell death mechanism formerly defined only by morphological changes in cells (Figure 1). At first, cells are shrinking due to loss of water. As a result, the organelles become more densely packed and the cytoplasm becomes denser. The next step is condensation of chromatin followed by separation of cell fragments into apoptotic bodies. An important feature is the retention of membrane and organelle integrity. The bodies are phagocytosed by macrophages. Unlike necrosis, apoptosis does not lead to inflammation because no cellular contents of apoptotic bodies are released, they are rapidly degraded, and no inflammatory factors are produced in response to phagocytosis. Since apoptosis can controllably destruct cells, it plays an important role in biological processes ranging from embryogenesis to aging, and from tissue homeostasis to a variety of human diseases like cancer. (18–21)

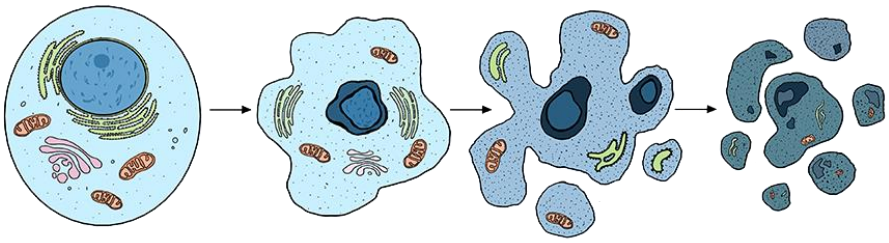

Figure 1: *Morphological change of the cell during apoptosis.*

Apoptosis can be divided into two phases: induction and execution. The induction phase is composed of death-inducing signals which simulate proapoptotic signal transduction cascades. Most of the proapoptotic genes activate a specific group of proteases known as caspases (cysteinyl-aspartate specific proteases). Caspases mainly regulate the execution phase of apoptosis due to their proteolytic activity. Their target molecules are cleaved at aspartic acid residue. However, there are two groups of caspases: initiators and effectors or executioners. Inactive caspases are composed of pro-apoptotic states which get activated through proteolytic cleavage. Hence, effector caspases get activated by initiator caspases which can be activated by two different pathways: the intrinsic or mitochondrial pathway, and the extrinsic or death receptor pathway (Figure 2). When cells are stressed (reactive oxygen species (ROS), DNA-damage) they generate intracellular signals which activate the intrinsic pathway. The mechanism is caused by the release of proteins like cytochrome c from the intermembrane space of mitochondria. There, cytochrome c binds to apoptotic protease-activating factor-1 and oligomerizes with procaspase-9 under conformational change, forming the so-called apoptosome. Thus, activation of the initiator caspase-9 takes place, which in turn activates the effector caspase-3 by cleaving the pro-caspase-3. Hence, cell death is induced by further caspase activities. In contrast, the extrinsic pathway is activated by formation of the death-inducing signalling complex which is generated by the attachment of extracellular death ligands such as the Fas ligand of natural killer cells to cell-surface death receptors. This autocatalytically activates procaspase-8 to caspase-8, which in turn activates caspase-3 and caspase-7. Moreover, caspase-8 can promote the release of mitochondrial cytochromes c via proteolysis of the pro-apoptotic Bcl-2 protein BID (BH3 interacting domain death agonist) to tBID, thus starting the intrinsic signalling pathway. (20, 22–25)

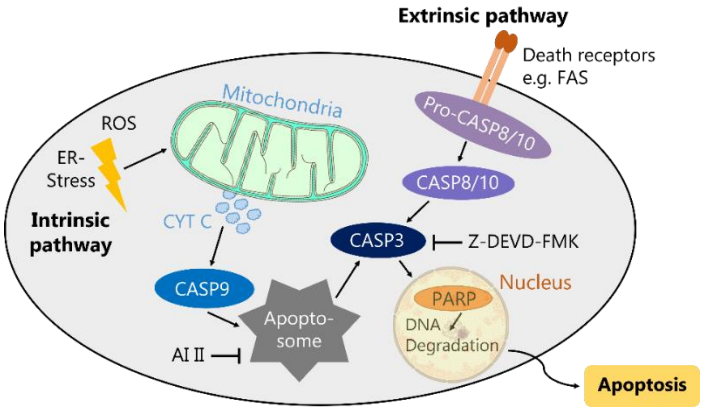

Figure 2: *Schematic illustration of extrinsic and intrinsic apoptosis pathways. (26)*

There are a variety of substances that induce or inhibit apoptosis. A common inducer is CisPt by DNA damage or paclitaxel as a microtubule-stabilizing agent. Because apoptosis relies on specific pathways, those can be targeted by apoptosis inhibitors. For example, apoptosis inhibitor II (AI II) inhibits apoptosome formation, while Z-DEVD-FMK inhibits caspase-3. (27–29)

1.2.1 Cisplatin

Since the approval of CisPt, cis-diaminedichloridoplatinum(II), in 1978, it is one of the most widely used anticancer agent for the treatment of numerous solid tumours like bladder, head and neck, lung, ovarian, and testicular cancer. Chemically, CisPt belongs to the group of DNA alkylating agents that are apoptosis inducers. Thus, the interaction with DNA, but also other biological nucleophiles including glutathione (GSH) or proteins leads to tremendous cytotoxic effect of the drug. CisPt itself is inert but it can be activated by several aquation reactions. Hence, one or both cis-chlorido groups are substituted for water molecules (Figure 3A). Once it is activated, the aquatic complex can bind to DNA, preferably at the nucleophilic N7-sites on purine bases. Thereby, DNA-DNA and protein-DNA inter- and intra-strand adducts are generated (Figure 3B). As a result, a permanent arrest of cell proliferation and cell death through apoptosis or necrosis is induced. (5, 30, 31)

Despite its success, CisPt has some drawbacks like severe side effects including emeto-genesis, neurotoxicity, ototoxicity, and the dose-limiting nephrotoxicity. These can be reduced by sufficient hydration of patients or circumvented by switching treatment to

carboplatin. Another limitation is the narrow range of tumour types susceptible for CisPt therapy. Additionally, intrinsic resistance to CisPt is an issue for some tumours, while others evolve acquired resistance after subsequent treatment. Therefore, the investigation of the generation of resistance and of side effects is very important to counteract them. (6, 32, 33)

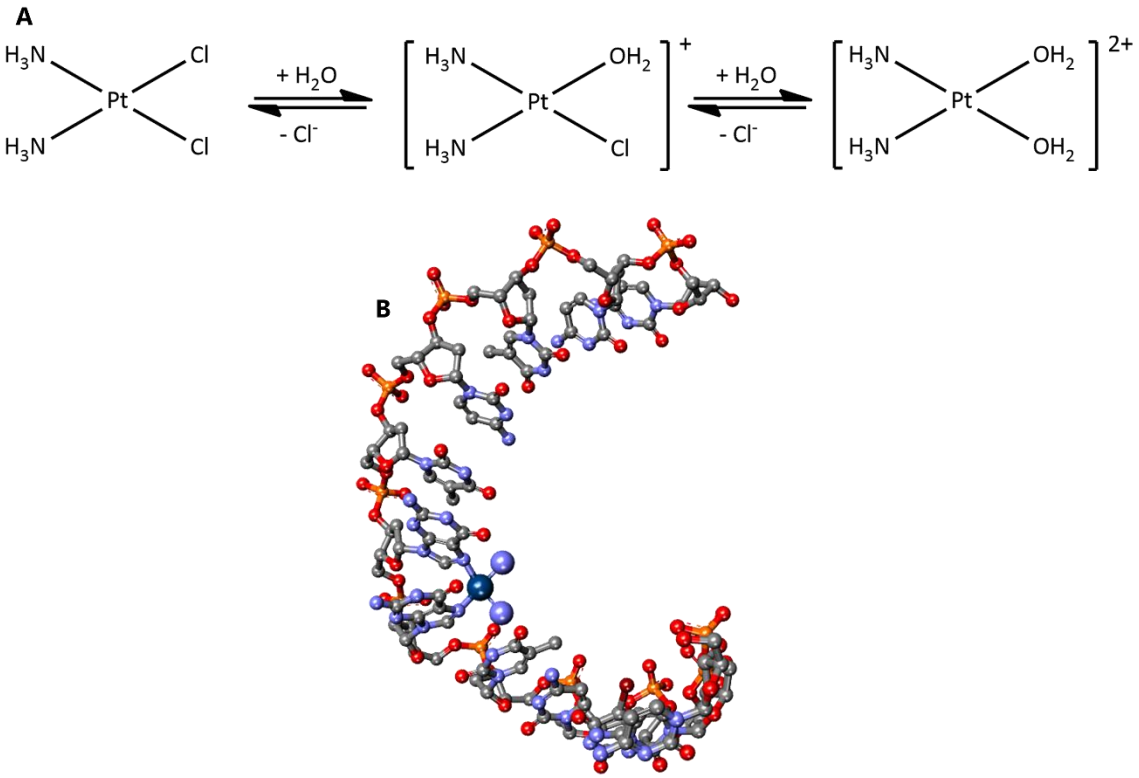

Figure 3: *(A) Formation of the platinum (II) aqua complex. (B) X-ray crystal structure of DNA - DNA intrastrand adduct with platinum (II) aqua complex. (34)*

1.3 Ferroptosis

In 2012, Dixon et al. coined the term ferroptosis, an iron-dependent, non-apoptotic RCD. It is characterised by the accumulation of lipid ROS and subsequent plasma membrane rupture. Ferroptosis is distinct from apoptosis, and necrosis due to biochemical, genetical, and morphological criteria. Morphologically, cells undergo mitochondrial shrinkage, increased membrane density, and reduction or vanishing of mitochondrial cristae. In comparison to other cell death mechanisms the cell membrane is still intact, there is no condensation of chromatin, and the nucleus is still normal sized. Biochemically, ferroptosis is the result of unrestrained lipid peroxidation in the mitochondrial membrane. As

a result, mitochondrial membrane fluidity is compromised, leading to inhibition of cellular respiration and thus to an adenosine triphosphate (ATP) crisis. Genetically, multiple genes regulate the biological process of ferroptosis. Therefore, iron homeostasis and lipid peroxidation metabolism underlie genetical changes. (4, 7, 8, 34)

However, ferroptosis is regulated by two activation mechanisms: the extrinsic or intrinsic pathway (Figure 4). The extrinsic pathway is induced by activation of the iron transporters lacto- and serotransferrin, enabling polyunsaturated fatty acids (PUFAs) to be oxidized by Fe^{2+} in a Fenton-like manner, or by the inhibition of cell membrane transporters such as the cytosine/glutamine transporter (x_c^-) leading to depletion of intracellular GSH. Alternatively, blockage of intracellular antioxidant enzymes like glutathione peroxidase 4 (GPX4) activates the intrinsic pathway by preventing lipid peroxides from being reduced by GPX4 and thus accumulating. (4, 8)

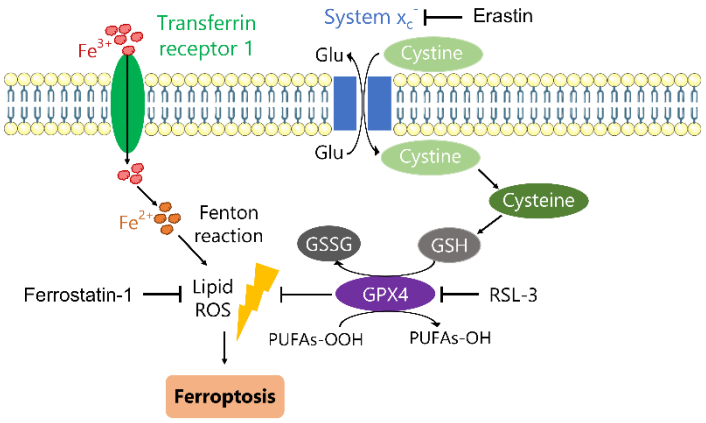

Figure 4: *Schematic illustration of ferroptosis pathways. (26)*

Ferroptosis, which occurs completely independent of apoptosis, is an auspicious therapeutic target for the treatment of cancer and many other diseases. A promising aspect is that cells classically resistant to apoptosis-inducing agents are sensitive to ferroptosis induction. Whereas, whether a particular cancer is resistant or more sensitive to ferroptosis relies on its genetic background, as numerous cancer-related genes and signalling pathways modulate ferroptosis. Consequently, these genes may serve as biomarkers by predicting the efficacy of ferroptosis-inducing therapies on cancer cells. (8, 35)

There is a big variety of substances which induce or inhibit ferroptosis. Common inducers are erastin (inhibits x_c^-). and (1S,3R)-RSL-3 (RSL-3, inhibits GPX4). Additionally, ferrostatin-1 (inhibits accumulation of lipid ROS) is a specific inhibitor of ferroptosis. The anti-

ferroptotic activity of ferrostatin-1 is based on the scavenging of alkoxyl radicals generated by iron in a catalytic manner. The inhibitor is not consumed in the process, as it is reduced by iron itself. (34, 36–38)

1.3.1 RSL-3

(1S,3R)-RSL-3 is a RAS-selective lethal compound, which can activate ferroptosis (Figure 5). The underlying mechanism is complex and not yet fully understood. The key function of RSL-3 induced cell death appears to be the inhibition of GPX4. Thereby, RSL-3 covalently binds to the allosteric side of GPX4, which initiates a conformational change. As a result, inhibition of GPX4 and ultimately cellular GPX4 protein degradation occurs. The activity of RSL-3 is independent of proliferation and does not require protein synthesis. Unlike apoptosis, induced cell death of RSL-3 is caspase independent. Additionally, RSL-3-induced death can be prevented by antioxidants like vitamin E or iron chelators. Thus, Fenton chemistry and intracellular ROS both play important roles. In approximately 30% of all cancers the RAS family small GTPases are mutated. Thus, it is very important to find compounds like RSL-3 that are selectively lethal to RAS-mutant tumour cells. (34, 37, 39–42)

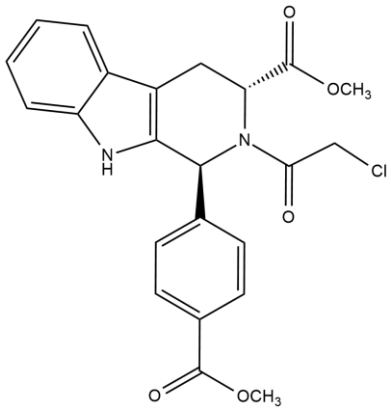

Figure 5: *Structure of (1S,3R)-RSL-3.*

1.4 Traditional biochemical assays to analyse cell death execution

Cell death execution of apoptosis and ferroptosis can be followed by classical biochemical assays. By determining cell viability, treatment concentrations can be obtained. The

annexin-V/propidium iodide (AV/PI) assay confirms whether the treatment has induced apoptosis in the cells. The dichloro-dihydro-fluorescein diacetate (DCFH-DA) assay provides important information weather ROS are involved in apoptosis or ferroptosis and the mitochondrial bioenergetics assay quantifies their ATP production.

1.4.1 AV/PI assay

This AV/PI assay is designed to measure plasma membrane integrity. Structural changes of cells during the process are used to detect their conditions: live, early apoptotic, late apoptotic, or necrotic. (43)

During an early apoptotic stage, cells are experiencing a change in plasma membrane structure. Thereby, phosphatidylserine (PS) is exposed at the surface while the membrane integrity remains intact. In healthy cells PS is a component of the plasma membrane which is actively detained to the inner membrane leaflet. The protein AV has a high affinity and selectivity for binding PS. Therefore, fluorescent labelled AV can detect externalised PS and thus early and late apoptotic cells. Normal vital and necrotic cells cannot be detected with AV since there is no PS present at the outer membrane leaflet. (44–47)

PI, a membrane impermeable DNA strain, is used to discriminate between early apoptotic and late apoptotic or necrotic cells. Due to their intact plasma membrane, live or early apoptotic cells cannot be stained with PI. The integrity of the plasma membranes declines in late apoptotic or necrotic cells. As a result, PI can pass through both membranes and intercalate into nucleic acids. Thus, fluorescence can be detected. The distribution between the two different fluorescence appearances reveals if cells are viable, early apoptotic, late apoptotic, or necrotic. (43, 48, 49)

1.4.2 Cell viability assay

The evaluation of cell metabolic activity was done via 3-(4,5-dimethylthiazol-2-yl)-2,5-diphenyltetrazolium bromide (MTT) staining method. In metabolically active cells, mitochondrial succinate dehydrogenase cleaves the tetrazolium ring, reducing yellow MTT to a water-insoluble purple formazan (Figure 6). In cellular cytosol the formazan precipitates

and is dissolvable after cell lysis. Thus, the MTT assay is mitochondrial respiration dependent and serves as an indirect evaluation of the cellular energy capacity of a cell. The exact mechanism is not yet completely understood. Finally, an organic solvent is used to dissolve the water-insoluble formazan. Now it can be measured spectrophotometrically with approximately 550 nm as an absorbance peak. Thus, the half maximal concentration of growth inhibition (IC_{50}) of CisPt and RSL-3 on tumour cells were determined. (50–53)

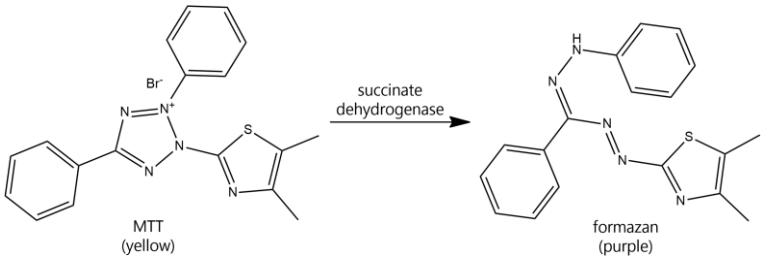

Figure 6: *Mechanism of activation of MTT to formazan.*

1.4.3 DCFH-DA assay

The cell-permeable fluorescent marker DCFH-DA is used for directly labelling intracellular ROS via flow cytometry. After the non-fluorescent DCFH-DA has readily crossed the membrane, intracellular esterases cleave the acetates. The non-fluorescent product of deacetylation is called 2`,7`-dichlorodihydrofluorescein (DCFH), which is polar and membrane-impermeable. Intracellular ROS subsequently oxidates DCFH, producing the highly fluorescent 2`,7`-dichlorofluorescein (DCF, Figure 7). The extent and rate of cellular ROS production can be quantified by quantifying the fluorescence signal. (54–56)

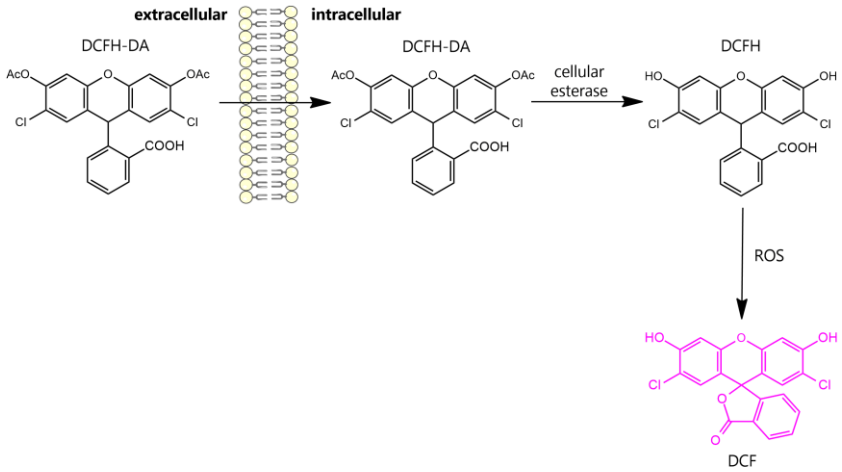

Figure 7: *Mechanism of DCFH-DA to DCF. (26)*

1.4.4 Mitochondrial bioenergetics

Since mitochondria are central actors in apoptosis and ferroptosis, the evaluation of mitochondrial bioenergetics is of great interest. The analysis was conducted using a real-time ATP rate assay. This assay allows quantification of ATP production from mitochondrial respiration and glycolysis via the detection of mitochondrial (mito) oxygen consumption rate (OCR) and glycolytic (glyco) extracellular acidification rate (ECAR). Two fluorophores are used to detect changes in O_2 and pH concentration over time. Moreover, oligomycin (OM), which inhibits the function of ATP synthase, and rotenone/antimycin-A (R/AA), which inhibits complex I and III, respectively, can be added during the assay. To determine mitoATP turnover, OM OCR is used. Here, a distinction is made between oxygen consumption by the natural proton leak at the inner mitochondrial membrane and oxygen consumption for ATP synthesis. In comparison, the application of R/AA results in the electron transport chain being completely inhibited. This allows the determination of glycoATP turnover rate. Finally, the total ATP production rate is calculated as the sum of mito- and glycoATP production rate. (57–59)

1.5 Omics technologies

Omics technologies are used to obtain a holistic picture of the molecules in biological samples such as cells, cellular components, tissues, or organisms. The omics cascade, which is shown in Figure 8, includes the universal detection of genes (genomics), RNA (transcriptomics), proteins (proteomics), and metabolites (metabolomics). Here, genomics describes the genotype in detail, whereas the qualitative and quantitative information of the metabolomics represent the phenotype, which reflects the functional state of the organism or cell. (60, 61)

Even though the individual steps of a workflow can differ greatly depending on the omics discipline, a general workflow can be described (Figure 9): The first step is sample collection, followed by sample preparation and analysis, and finally data analysis. For metabolomics and proteomics, these steps will be discussed later in more detail. (62)

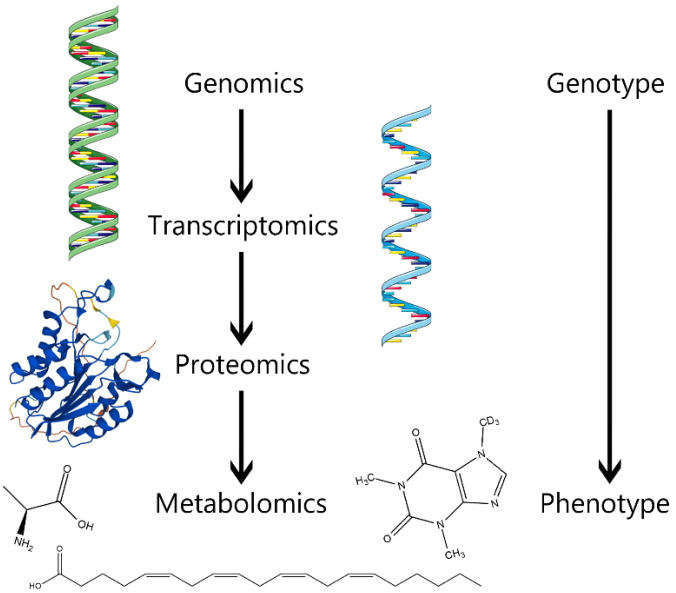

Figure 8: *Overview of an omics cascade starting with the first discipline, genomics, on through transcriptomics and proteomics to metabolomics. (26, 63)*

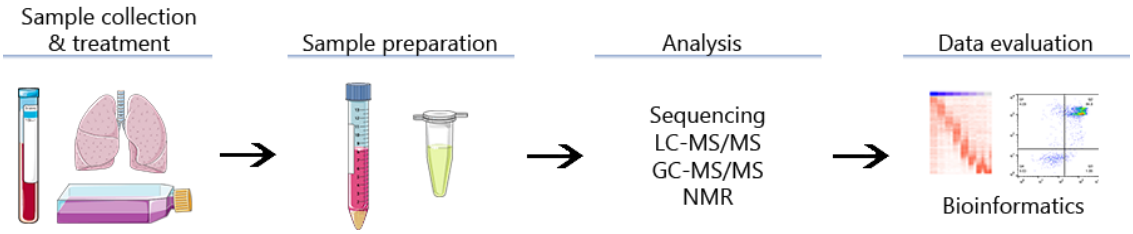

Figure 9: *Overview of a general omics workflow. (26)*

1.5.1 Proteomics

In general, proteomics describes the large-scale analysis of proteomes. The term proteome refers to the totality of all expressed proteins in a specific organism, tissue, or cell at a given time point. Thus, proteomic analyses are used to identify and quantify all proteins and their proteoforms including isoforms, post-translational modifications (PTMs) and splicing variants. This allows the cellular localization of proteins and the determination of their turnover rates as a function of cell type, external stimuli, and time. (64, 65)

Nowadays, the bottom-up method, also known as shotgun proteomics, is the most widely used proteomic approach. Thereby, the proteins are completely proteolytically digested prior to mass spectrometry (MS) analysis. This requires proteases such as trypsin, which break down proteins into short peptides. The serine protease trypsin is not only highly specific but also cleaves at the carboxyl side of arginine and lysine residues.

Since the resulting C-terminal arginine and lysine peptides are charged, they can be detected by MS analyses. Since both the cleavage sites of the proteolytic enzymes and the masses of the amino acids are known, *in silico* digestion of proteins can be conducted. As a result, the masses of all theoretically generated peptides are obtained. Next, search algorithms are applied so that experimentally determined mass-to-charge ratio (m/z) values and spectra can be assigned to peptide candidates. This is accomplished by comparing the measurement results with the theoretical masses and spectra in public databases such as UniProt. Finally, proteins can be identified by peptide spectrum matches. (64, 66, 67)

A popular quantification method for shotgun proteomics is label free quantification (LFQ), which can be divided into two different methods: The first approach uses the intensities of precursor ions of certain peptides. To estimate protein concentration, the area of chromatographic peaks of several or all peptides associated with one protein is measured. In addition, there is the method of spectral counting, which involves counting the number of MS/MS spectra for a given protein. This approach is controversial and generally achieves less accurate quantification results than the first method. (64, 68)

Shotgun proteomics can be generally divided into untargeted and targeted approaches. In untargeted proteomics, the aim is to obtain broad coverage of the proteome in a sample, i.e., to identify and/or quantify as many proteins as possible. In comparison, the targeted approach focuses on specific proteins that are pre-defined. (69)

The rapid development of bioinformatics and MS has led to a steady improvement of the proteomics workflow, ensuring high accuracy, resolution, and sensitivity. Since proteomics can be used to study cellular signalling pathways and protein interactions, it is a powerful tool for studying various diseases and identifying drug targets. (67, 70, 71)

In bioinorganic anticancer drug discovery, protein target identification is still a challenge. Tailored proteomic approaches can identify potential protein targets of metal-based drugs. This method has demonstrated that metal-based drugs can engage selectively and sometimes even highly specifically on protein targets in cells. In addition, proteomic analysis can also be used for the study of drug-activity profiles and modes of action. (72–74)

1.5.1.1 Phosphoproteomics

Phosphoproteome analysis provides information on the regulatory pathways of protein phosphorylation and dephosphorylation, which is a ubiquitous PTM and plays an important role in various diseases. Thanks to continuous improvement in sample preparation, phosphorylation enrichment, quantification, and data analysis strategies, it is possible to perform both targeted and ultra-deep phosphoproteome profiling. Since MS provides highly sensitive analysis and quantitative as well as site-specific measurements, it is ideal for the examination of protein phosphorylation. However, it should be noted that there are still some limitations such as potentially impaired digestion efficiency, phosphopeptide losses during both sample preparation and chromatography, and impaired ionization efficiency of phosphopeptides. Phosphorylation and dephosphorylation of proteins consist of highly dynamic, rapid cascade processes. Capturing phosphorylation and dephosphorylation events that occur in a specific disorder in in vitro or even in vivo models is not an easy task. Such dysregulations are often associated with various diseases such as cancer, diabetes, or neurological diseases. Kinases are frequently used as drug targets of cancer therapies as they are involved in the carcinogenesis of various types of cancer. To gain a better insight into cellular signalling, it is crucial to identify phosphorylation sites. In addition, conclusions can be drawn about enzymes and phosphorylation sites relevant to the diseases. (75–80)

1.5.2 Metabolomics

The term metabolomics describes the qualitative and quantitative analysis of the metabolome in a biological system. The metabolome consists of the complete set of metabolites in a specific organism at a given time point. Moreover, metabolic profiles not only represent endogenous metabolites but also contain exogenous metabolites originating from diet, drug, and gut microbiota. Thus, metabolomics is the analysis of small molecules such as amines, amino acids, carbohydrates, lipids, nucleotides, peptides, steroids, vitamins, and other intermediary metabolites. Because metabolites are the end product of gene expression, they present immediate snapshots of the physiology of the cell or organism. Due to environmental stress such as exercise or diet, metabolites can change

rapidly (seconds to minutes). Hence, metabolomics analysis determines novel biomarkers, highlights biological information about the physiological state of an organism and provides potential therapeutic targets. Nuclear magnetic resonance, gas or liquid chromatography mass spectrometry (LC-MS) are often used to analyse the metabolites. (81–84)

Metabolomic analysis can be divided into two experimental workflows: non-targeted and targeted metabolomics. Non-targeted studies, or metabolic profiling, aim to detect as many metabolites as possible without prior knowledge of the nature of the metabolites. Therefore, non-targeted metabolomics gains only qualitative and semi-quantitative information but is widely applied in hypothesis generating studies such as biomarker discovery. In comparison, targeted studies refer to the precise quantification of a selected group of expected and known metabolites. This allows the investigation of a specific metabolic pathway, or the validation of biomarkers identified by metabolic profiling. To achieve high accuracy, precision, and specificity, sample preparation and optimal instrument setup are very important. In contrast, targeted metabolomics are often more quantitative, whereas non-targeted studies typically provides more information. (81, 83, 85)

Metabolomics provides a comprehensive and dynamic picture of the phenotype that can be used to develop effective therapeutic interventions. Thereby, new information on mechanisms of action of drugs can be investigated, and drug efficacy and safety can be predicted. In addition, the analysis of the metabolome can be consulted for the diagnosis or prediction of diseases. (86–88)

1.6 Liquid chromatography – mass spectrometry

The design of LC-MS essentially consists of a pump system, an injector and a column connected to the mass spectrometer via an evaporative ionization interface. Technological developments in LC-MS over the last two decades enabled the rapid growth of proteomics and metabolomics techniques. (89, 90)

1.6.1 Liquid chromatography

LC is a chromatographic separation method based on the distribution of analytes between a liquid mobile phase and a solid stationary phase. Different separation processes can be obtained depending on the combination of the two phases. Moreover, the separations by size (size exclusion chromatography), by ionic strength (ion exchange chromatography), by polarity (reversed-phase (RP) chromatography) and by hydrophilicity (hydrophilic interaction liquid chromatography, HILIC) are most commonly used. In this work, a C18 RP column was used as the material of choice. Generally, RPLC is used for peptide analysis and HILIC for small polar compounds such as metabolites. (89, 91)

An alternative to LC is nano LC. There is no generally accepted definition for this method, but the characteristics that the inner diameter of the capillary measures 10 to 100 µm and a low flow rate of <1 µl/min is applied is most commonly used. This method provides many advantages like an increased separation efficiency and a smaller consumption of mobile phase. Furthermore, a smaller sample volume is required. This is especially important for studies of biological samples, as these are often limited. In addition, the lower flow rate together with the small column diameter causes a smaller chromatographic dilution, resulting in higher sensitivity and lower variability. Coupling nano LC with electrospray ionization (ESI) leads to increased ionization efficiency by reducing ion suppression and matrix effects to a minimum. (92)

1.6.2 Mass spectrometry

MS is an analytical technique in which ionized molecules get separated according to their m/z under high vacuum. In MS analysis, analytes can be measured either directly (MS^1), providing the exact mass, or pre-fragmented (MS^2), which allows indirect identification of the structure. Due to the larger dynamic range of the MS^1 spectrum compared to MS^2, the MS^1 areas are primarily used for quantification. Through the combination of chromatographic (retention time) and mass spectrometric information, the analytes can be identified and even quantified. (90, 93, 94)

A mass spectrometer generally consists of an ion source in which molecules are ionized, a mass analyser that separates the ions according to their m/z ratio, and finally the detector in which the separated ions and their abundances are recorded. For metabolomics and proteomics, the most common mass analysers are Fourier-transform ion cyclotron resonance instruments, ion traps, Orbitrap analysers, quadrupole mass filters (Q) and time-of-flight instruments (TOF). Nowadays, hybrid instruments such as Q-ion mobility-TOF, Q-TOF, Q-Orbitrap, and QQQ are usually used. (95, 96)

Modern ion mobility mass spectrometry (IMMS) enables highly selective measurements due to ion funnels and traps, which trap and refocus the ions before they are injected into the MS analyser. An enormous reduction of the proportions of IM analysers was achieved through the invention of trapped ion mobility spectrometry (TIMS) instruments. Here, the ions are held in the drift cell by applying an electric field against a counter gas flow. Quadrupoles and collision cells are usually used between the TIMS analyser and the MS analyser. (97)

Since all measurements for this work were performed on either the Q Exactive™ HF Hybrid Quadrupole-Orbitrap™ mass spectrometer or the timsTOF™ Pro, the specific setup of these two devices will now be discussed in more detail.

1.6.3 Q Exactive™ HF Hybrid Quadrupole-Orbitrap™

The Q Exactive™ HF mass spectrometer features a prefilter, high performance quadrupole and an ultra-high field Orbitrap™ analyser. Moreover, the introduction of Q Exactive™ revolutionized the field of proteomics by allowing a much higher number of proteins to be analysed per hour. Figure 10 shows the setup of the Q Exactive™ HF Hybrid Quadrupole Orbitrap™, which consists of the following: an atmospheric ion source, a stacked-ring ion guide (S-lens), an advanced active beam guide with an injection flatapole and a bent flatapole, a hyperquad mass filter with advanced quadrupole technology (mass filter), a C-trap, a higher-energy collisional dissociation (HCD) cell and an Orbitrap™ mass analyser. (98, 99)

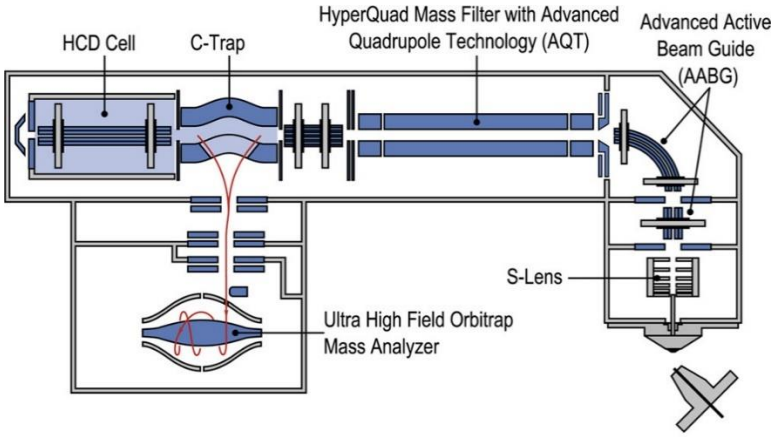

Figure 10: *Structure of Q Exactive™ HF Hybrid Quadrupole-Orbitrap™. (98)*

After separating the analytes by HPLC, the molecules are ionized and transferred to the gas-phase via ESI. Subsequently, the ionized analytes pass through the S-lens, injection flatapole and the bent flatapole, where unwanted ions such like uncharged molecules and remaining solvent droplets are removed. The remaining ions are transferred to the quadrupole, which acts like a mass filtering device. Pre-filtering prevents contaminants from reaching the rods of the quadrupole, which in turn increases the robustness of the instrument. A linear quadrupole consists of four hyperbolic parallel-paired rod electrodes, with each opposing pair of electrodes electrically connected. The special feature of the advanced quadrupole technology of the Q Exactive™ HF Hybrid Quadrupole Orbitrap™ mass spectrometer is the segmented quadrupole mass filter, which enables a more precise precursor isolation efficiency over the isolation window. Next, the ions are transferred through a short octopole into the C-trap, where they can be accumulated and stored. Now the ions can either be transferred directly into the Orbitrap™ for analysis, or they can enter the HCD cell for fragmentation. The HCD cell consists of a multipole collision cell where ions dissociate by colliding with neutral gas molecules like nitrogen gas under a certain collision energy. The fragments are then returned to the C-trap and on to the Orbitrap™ analyser. The ions oscillate in the Orbitrap™ around an inner spindle-shaped electrode, which is held at constant voltage. The resulting image current is recorded. Since the ions oscillate at different frequencies depending on their m/z values, a fast Fourier transformation can be used to determine their m/z values. The analysis of the m/z values of the fragmented ions is called MS^2, whereas MS^1 analysis consists of measuring the non-fragmented ions transferred directly from the C-trap to the orbitrap™. The use of the Q Exactive™ HF Hybrid Quadrupole Orbitrap™ mass spectrometer

results in an increase in ion transmission, isolation efficiency, resolution, and robustness. Metabolomics analysis for this work was performed using such an instrument. (95, 98–100)

1.6.4 timsTOF™ Pro

The IMMS instrument TimsTOF™ Pro features a dual TIMS analyser with an ultrahigh-resolution-TOF (Figure 11). The instrument consists of the following: an atmospheric ion source, a double-focusing entrance funnel, a dual TIMS analyser, a transfer multipole, a segmented Q, a collision cell and an TOF mass analyser. (101)

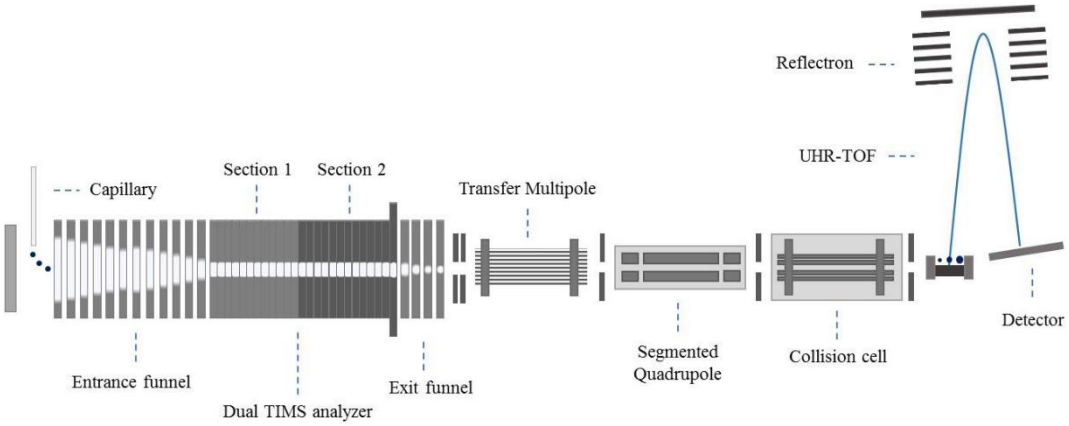

Figure 11: *Structure of timsTOF™ Pro. (102)*

First, the sample is ionized by an ESI source and the desolvated ions are transported through an orthogonal glass capillary where they are rotated 90°. Next, they are passed through an electrodynamic double-focusing entrance funnel into the dual TIMS analyser. The TIMS tunnel consists of a stacked multipole in which the trapped ions are radially confined by the application of a RF potential. With a force proportional to their collision cross-section, the injected ions are pushed forward by a gas flow in the TIMS analyser. The applied RF field is superimposed by an increasing longitudinal DC field gradient from the entrance to the exit. Thereby, the ions are pulled forward by the gas flow and repelled by the opposing electric field. The ions are held at the point where the opposing electric field and the force of the gas flow are equal, depending on their charge state and the values of their collision cross sections. Ions are trapped at different positions along the TIMS tunnel since the resistance of the gas stream is proportional to the collision cross sections of an ion. This results in the high mobility ions coming to rest closer to the

entrance and the low mobility ions coming to rest closer to the exit. In the second section of the TIMS tunnel, ion mobility based separation and analysis takes place, whereas in the first section new ions can already be collected, stored and pre-separated according to their ion mobility. By lowering the electric field gradient linearly, the stored ions are released from the TIMS analyser. Due to their smaller collision cross section relative to their charge, low mobility ions elute before high mobility ions. (97, 101, 103)

The ions are now transferred into the segmented quadrupole through a focusing output funnel and a transfer multipole. In the quadrupole, the m/z values can be filtered for the selection of the precursor ions (MS/MS scan). Next, the ions enter the collision cell, where the ions are accelerated. In addition, the ions are either transferred further without fragmentation (MS scan) or fragmented by collision with an inert gas (MS/MS scan). Then the ions are transferred into the orthogonal accelerator unit, where ion packages are formed. These are ejected into the drift tube where they are analysed under field free conditions. The ions fly a V-shaped path where they are reflected by a two-stage reflectron. This causes the kinetic energy distribution of the ions to be compensated. Finally, the ions are detected by a multi-channel plate ion detector. The additional separation by ion mobility enables isomeric and isobaric compounds to be distinguished. Thus, clean MS/MS spectra are obtained after compound separation and fragmentation. The robustness of the device is increased by deflecting the ions 90° at the entrance of the device and an improved quadrupole design. The timsTOF™ Pro offers not only a high mass resolution of up to 200 but also a high mass accuracy in the low ppm range. High specificity can be ensured by combining accurate collision cross section values (<0.5% relative standard deviation) and clean MS/MS fragmentation spectra. For this work, phosphoproteomics analysis was performed using a timsTOF™ Pro. (97, 101, 104)

2 Aims & objectives

Preliminary experiments of LFQ proteomics had already been performed to confirm caspase activation during apoptosis and whether any endoprotease would be activated during ferroptosis. For this purpose, A2780 ovarian cancer cells were treated with CisPt

and RSL-3. Caspase activation was confirmed upon apoptosis induction, but ferroptosis was proteolytically silent (Figure 12). (105)

In addition, Figure 13 reveals that caspase 3 (32 kDa) was itself proteolytically activated during apoptosis induction, as its peptides were found in subunits of lower molecular weight (2-20 kDa). In contrast, caspase 3 was not cleaved and thus not activated upon ferroptosis induction cells.

In summary, apoptosis has clear effects on the level of the proteome due to the activation of caspases, whereas ferroptosis showed no such effect. Consequently, it is hypothesized that ferroptosis must manifest in some other ways that remain to be explored.

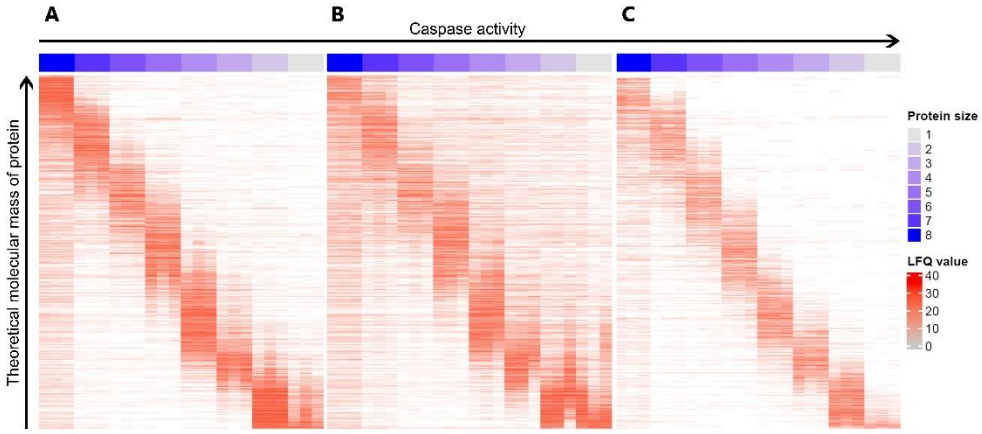

Figure 12: *Heatmap of electrophoretically separated proteins prior to LFQ proteomic analysis found in (A) untreated, (B) CisPt treated and (C) RSL-3 treated A2780 cells.*

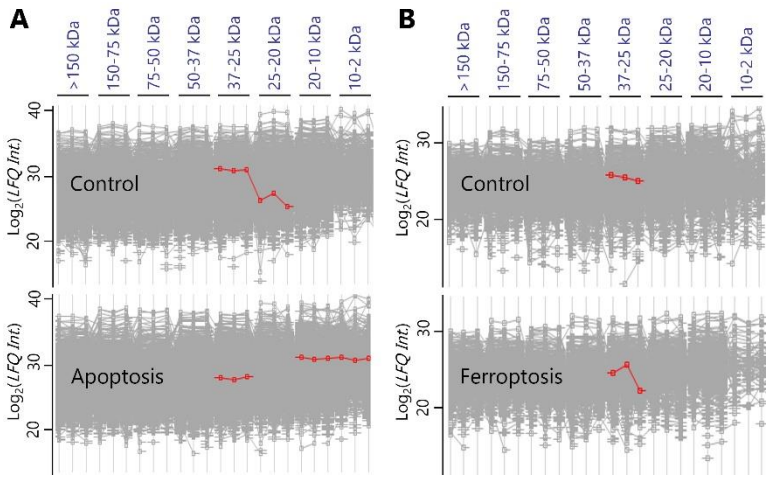

Figure 13: *Profile plots of caspase-3 in A1780 cells treated with (A) CisPt and (B) RSL-3. The profile of the control group is shown at the top and that of the treated cells at the bottom.*

The aim of this work was to comprehensively characterise apoptosis and ferroptosis mechanisms at the molecular level and to highlight similarities and differences between

the two cell death mechanisms. Therefore, a variety of traditional biochemical assays were applied, including AV/PI assay, cell viability assay, DCFH-DA assay and the analysis of the mitochondrial bioenergetics. Since ferroptosis does not seem to involve protease activity as apoptosis, the study of cellular signalling processes by means of metabolites and phosphopeptides may add substantial new insights into the molecular mechanisms of ferroptosis. Therefore, non-targeted metabolomics was performed to detect metabolic changes in the supernatant in both cell death mechanisms. In addition, LFQ phospho-proteomics was performed to identify phosphosites regulated by the two cell death mechanisms. A summary of the comprehensive workflow for the master's thesis is shown in Figure 14.

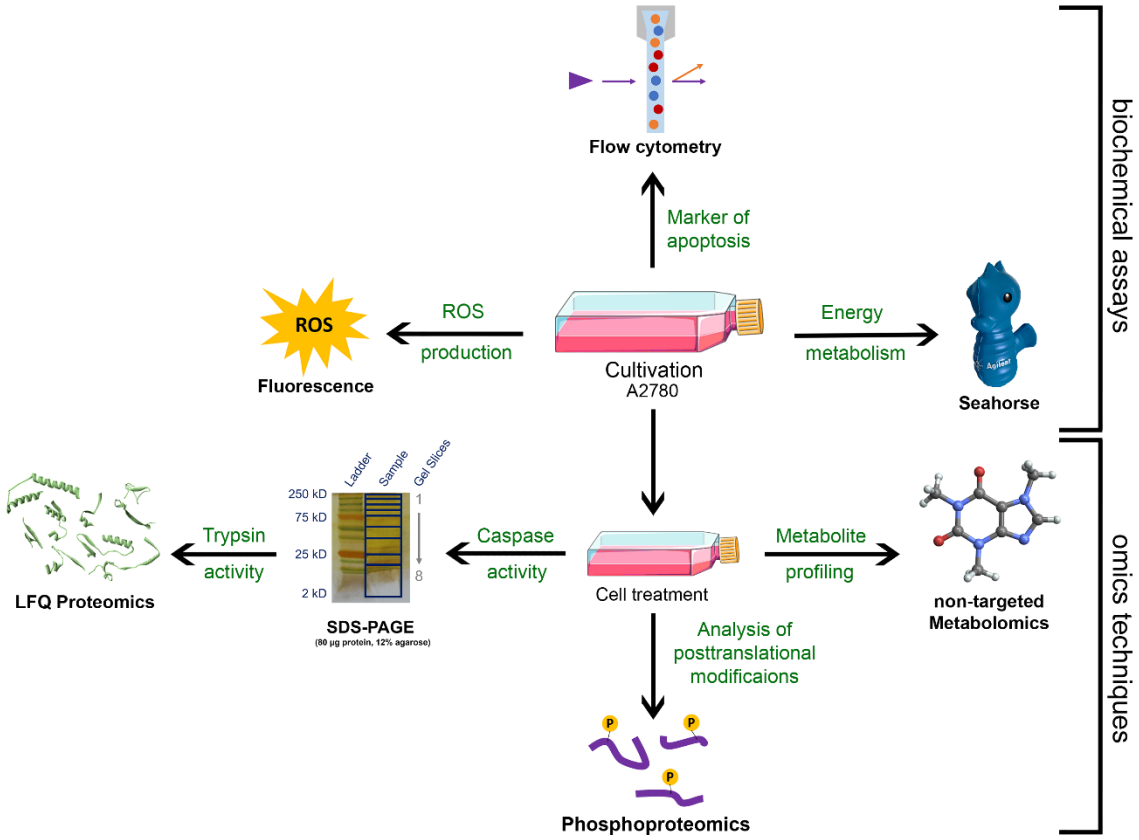

Figure 14: *Schematic of the workflow. A2780 cells were treated with CisPt or RSL-3 and undertaken traditional biochemical assays together with metabolomic and proteomic and phosphoproteomic analysis. (26)*

3 Materials & methods

3.1 Cell culture

Human ovarian cancer cells of the cell line A2780 were used to determine apoptotic or ferroptotic processes. The cells were kindly provided by Lloyd R. Kelland, CRC Center for Cancer Therapeutics, Institute of Cancer Research, Sutton, United Kingdome and Thomas Grunt, Medical University of Vienna. A2780 were grown in RPMI-1640 medium (RPMI, Sigma-Aldrich) supplemented with 10% heat-inactivated fetal bovine serum (FBS, Biowest), 4 mM L-glutamine (Sigma-Aldrich) and 1% antibiotic solution (penicillin-streptomycin, Sigma-Aldrich). Cultures were maintained as monolayers in 75 cm^2 culture flasks (T75, Starlab) at 37 °C in a humidified atmosphere of 5% CO_2 in air (Heracell 150i CO_2 Incubator, Thermo Scientific). Cells were regularly split in a range of 1:6 to 1:8 when they reached a confluency of approximately 75% to ensure proper growth. Therefore, the flask was washed twice with 3 ml of phosphate buffered saline (PBS, Sigma-Aldrich) after removing the old medium. Next, 2 ml of trypsin-EDTA solution (2.5 g porcine trypsin and 0.2 g EDTA, Sigma-Aldrich) was added and the flask was incubated for 5 min to allow the cells to detach. After incubation, cells were suspended in 8 ml medium, transferred to a Falcon tube, and centrifuged for 5 min at 1100 rpm and 23°C. Afterwards, the supernatant was discarded, and the pellet was resuspended in 2 ml medium. 10 ml of medium was added to the old T75 flask. Depending on how densely the flask was populated, 1:6 to 1:8 of the 2 ml cell suspension was added to the flask and the cells were placed back in the incubator.

3.2 AV/PI assay

At first, 600 µl of cell suspension per well was seeded into a 24-well plate at a density of 7×10^4 cells. In the first 24 h, the cells were allowed to settle and resume exponential growth at 37 °C and 5% CO_2. Afterwards, 600 µl of the treatment solutions were added as shown in Table 2 and incubated for another 24 h at 37 °C and 5% CO_2. Adding medium to the cell suspension was used as a negative control. As positive control, two concentrations, 0.5 µM and 0.25 µM, of TM-1 (compound 1-P from (106)) were prepared. Cells

were treated with three different concentrations (1/2×IC_{50}, IC_{50} and 2×IC_{50}) of either CisPt (KP-1, charge 6, synthesised by the Department of Inorganic Chemistry, University of Vienna) or RSL-3 (Sigma-Aldrich). Due to the dilution step, the concentrations of the treatment solutions must be twice the IC_{50} concentrations, determined in a previous experiment by Dr. Samuel Meier-Menches (Department of Analytical Chemistry, University of Vienna) and used for apoptosis and DCFH-DA assay (Table 1).

Table 1: *Overview of the IC_{50} concentrations of CisPt and RSL-3 after 24 h of incubation used for apoptosis and DCFH-DA assay.*

	CisPt [µM]	**RSL-3 [µM]**
2×IC_{50}	35.00	0.096
IC_{50}	17.50	0.048
½×IC_{50}	8.25	0.024

Table 2: *Overview of the used treatment pattern of the AV/PI assay.*

	A	**B**	**C (CisPt)**	**D (RSL-3)**	**E**	**F**
1	-control	+control (0.50 µM)	2×IC_{50}	2×IC_{50}		
2	-control	+control (0.25 µM)	IC_{50}	IC_{50}		
3			½×IC_{50}	½×IC_{50}		
4						

After exposure for 24 h, 5 ml Eppendorf tubes were used to collect all supernatants separately. The wells were washed with 500 µl PBS and the solutions were added to the corresponding tubes. Then, the plate was incubated with 200 µl Trypsin-EDTA solution per well for 4 min at 37 °C and 5% CO_2. After that, 600 µl of medium was added and the lysed cells were reunited with the supernatant. After centrifugation for 3 min at 1200 rpm, the supernatant volume was reduced to 900 µL per sample which was used to resuspend the pelleted cells, transferred into fresh Eppendorf tubes, and centrifuged at 2.1 rpm for 3 min. The supernatants were discarded and the pellets resuspended with 150 µl of fluorescein-5-isothiocyanate-conjugated AV (Invitrogen) in binding buffer (BB, Table 3) (2 µl AV + 150 µl of BB per well) and incubated for 15 min at 37 °C and 5% CO_2. Then, 150 µl of 9,97 µM PI solution (1 µl of 1 mg/ml PI (Sigma-Aldrich) + 150 µl of BB per well) were added to each well. The plate was measured with a Millipore guava easyCyte™ 8 HT flow cytometer and InCyte software. Further analysis of the received dot plots was performed

by FlowJo software (v.10.6.1, TreeStar). The AV/PI assay was performed in at least three individual experiments.

Table 3: *Composition of the binding buffer in 200 ml Milli-Q water.*

Chemicals	c [mM]	M [g/mol]	m [g]
Hepes/NaOH, pH 7.4 (Thermo Scientific)	10.0	238.32	0.47662
NaCl (Sigma-Aldrich)	140.0	58.50	1.63800
$CaCl_2$ (Sigma-Aldrich)	2.5	111.00	0.05550

3.3 Cell viability assay

Cell viability assays were performed with and without inhibitor. A total of 2×10^3 cells per well were seeded into a 96-well plate, which corresponds to 100 µl of the cell suspension plus inhibitor (Table 5) per well. Then, the plate was incubated for 24 h at 37 °C and 5% CO_2. The next day, 100 µl of the test compounds per well were added in triplicate according to Table 4, followed by an incubation step for 96 h at 37 °C and 5% CO_2. Empty wells without cell suspension were used as blanks. Adding medium to the cell suspension was used as a negative control. Cells were treated with nine different concentrations of both CisPt (0.049 - 0.098 - 0.0195 - 0.391 – 0.781 – 1.563 – 3.125 – 6.250 -12.500 µM) and RSL-3 (0 38 – 0.76 – 1.53 – 3.05 – 6.10 – 12.21 – 24.41 – 48.83 - 97.66 nM). Thereby, the same concentrations were applied for the plates with and without inhibitor. Due to dilution, the concentrations of the treatment solutions must be twice as high.

Table 4: *Overview of the used treatment pattern of the MTT assay. The first column was empty. The negative control was added to the second one. The serial dilutions of CisPt and RSL-3 were applied at the columns C to K, starting with the lowest concentration at column C and ending with the highest concentration at column K. Three replicates were used for each compound.*

	A	B	C	D	E	F	G	H	I	J	K	L
1												
2												
3			*lowest*			CisPt					*highest*	
4		-control										blank
5												
6			*lowest*			RSL-3					*highest*	
7												
8												

Table 5: *Overview of the used inhibitors.*

Inhibitors	c [µM]
Ferrostatin-1 (Sigma-Aldrich)	5
Apoptosis inhibitor II (Merck)	50
Z-DEVD-FMK (Tocris)	20

After the 96 h treatment, the solution of each well was replaced with 100 µl of 1:7 MTT (250 mg of MTT (98%, Acros Organics) dissolved in 50 ml PBS/ RPMI mixture (with 10% heat-inactivated FBS and 4 mM L-glutamine). After 4 h of incubation at 37 °C and 5% CO_2 the wells were emptied and 150 µl dimethyl sulfoxide (Fisher Scientific) per well were added to dissolve the formazan crystals formed by viable cells. Lastly, the optical densities were measured spectrophotometrically at a wavelength of 550 nm with 690 nm as a reference with a microplate reader (ELx808, Bio-Tek). The cell viability assay was performed in at least three individual experiments. In addition, a slightly adapted 24h incubation method was also performed in another laboratory. IC_{50} values were determined from sigmoidal fitting. These new IC_{50} values were used for all further experiments except apoptosis or DCFH-DA assay.

3.4 DCFH-DA assay

The first experiment was performed without poly-L-lysin coated wells. As a result, the cells got washed away during the washing steps. Consequently, poly-L-lysin (Sigma-Aldrich) coated wells were used for the following experiments. For this assay, phenol-red-free Opti-MEM (1×, + 1% FBS, Gibco) was used as medium. Since a preliminary experiment showed that ROS activity is too low when the inhibitor (ferrostatin-1; 5 µM per well) is applied together with the dilution series treatment (CisPt and RSL-3) solution, the inhibitor was added during cell seeding in all experiments.

Next, 100 µl of cell suspension with a density of 25×10^3 cells per well were seeded into a 96-well plate and the plate was incubated for 24 h at 37 °C and 5% CO_2. Afterwards, the wells were washed with 200 µl of hanks balanced salt solution (HBSS, supplemented with 1% FBS, Sigma-Aldrich) and 100 µl of 25 µM DCFH-DA solution (Sigma-Aldrich) was added to each well followed by 45 min incubation at 37 °C and 5% CO_2. Then, the wells were once more washed with 200 µl HBSS (+ 1% FBS). Subsequently, cells were treated

with three different concentrations (1/2×IC_{50}, IC_{50} and 2×IC_{50}) of CisPt and RSL-3 (Table 6). Medium without cell suspension was used as blank. As a negative control, medium was added to the cell suspension. Two concentrations, 200 and 400 µM, of tert-Butyl hydroperoxide (TBHP, Sigma-Aldrich) were prepared as positive controls. The fluorescence measurement with Synergy HT reader (Bio Tek) was started immediately after adding the compounds at 485 nm (excitation) and 516 nm (emission) wavelengths and was repeated periodically every 10 min for 2 h. The DCFH-DA assay was performed in at least three individual experiments.

Table 6: *Overview of the used treatment pattern of the DCFH-DA assay (except the first experiment).*

	A	B	C	D	E	F	G	H	I	J	K	L
1	blank	-con	+con 400	CisPt			-con	+con 400	CisPt			
2				1/2×IC_{50}	IC_{50}	2×IC_{50}			1/2×IC_{50}	IC_{50}	2×IC_{50}	
3												
4												
5			+con 200	1/2×IC_{50}	IC_{50}	2×IC_{50}		+con 200	1/2×IC_{50}	IC_{50}	2×IC_{50}	
6												
7												
8				RSL-3					RSL-3			
		without inhibitor					with inhibitor					

3.5 Mitochondrial bioenergetics

Mitochondrial bioenergetics were measured by Seahorse XF HS Mini (Agilent) with an induced real-time ATP rate assay. Therefore, 80 µl of cell suspension were seeded into an 8-well plate for a total of 6×10^4 cells per well. Two wells were used as blanks, thus 80 µl RPMI without cells were added. After resting for 1 h at room temperature, the plate was incubated for 24 h at 37 °C and 5% CO_2. Additionally, the Seahorse XF cartridge was hydrated by adding 200 µl sterile H_2O per well and 400 µl sterile H_2O per moat. The cartridge was incubated overnight in a static incubator (Thermo Fisher Scientific) at 37 °C without CO_2 together with an aliquot of Seahorse XF Calibrant Solution (Agilent). The assay medium was prepared by mixing 9.7 ml Seahorse XF DMEM medium (Agilent) with 0.1 ml XF glucose solution (Agilent), 0.1 ml XF pyruvate solution (Agilent) and 0.1 ml XF glutamine solution (Agilent). This prepared assay medium was incubated overnight at 37 °C and 5% CO_2. The next day, H_2O was removed from the cartridge and 180 µl of

calibrant solution was added per well. Then, the cartridge was incubated for 1 h at 37 °C and no CO_2. The wells of the cell plates were washed: 60 µl of supernatant was removed and 160 µl of assay medium was added. Thereafter, all the medium was discarded, 160 µl was applied and the well plate was incubated for 1 h at 37 °C and 5% CO_2. After the incubation period, the injection ports on the cartridge were loaded. For this purpose, 20 µl of assay medium (blank) or treatment solution (10×IC_{50} concentration of CisPt or RSL-3) was added to port A. Port B was used to inject 22 µl of 15 µM OM solution (Sigma-Aldrich). Lastly, 25 µl of 12.5 µM R (Sigma-Aldrich) AA (Sigma-Aldrich) mixture (1:1) was added to port C. The analysis was started immediately after injecting the ports.

For this assay, the measurement of ECAR and OCR was conducted before (basal condition) and after administration of various metabolic stressors. After 18 minutes of basal condition measurement, the treatment solution was injected, followed by a 4 h incubation period with hourly measurement of ECAR and OCR. Subsequently, OM was added and after three measurement cycles, R/AA was injected and measured as well in three cycles. Treatment duration was determined in a preliminary experiment in which the cellular response to either treatment of CisPt or RSL-3 at respective IC_{50} concentrations was visually observed for 6 h, whereupon the timepoint of 4 h was chosen. The results were analysed by Origin 2022.

3.6 Metabolomics

3.6.1 Cell treatment

Firstly, 12 25 cm^2 culture flasks (T25, Starlab) were each filled with 5 ml of cell suspension at a density of 1×10^6 cells followed by an 24 h incubation step at 37 °C and 5% CO_2. The next day, the medium was exchanged with treatment solution as follows to obtain four replicates per condition: pure RPMI as control or RPMI spiked with IC_{50} concentrations of either CisPt (9 µM) or RSL-3 (0,106 µM). All flasks were incubated for 24 h at 37 °C and 5% CO_2.

3.6.2 Cell fractionation

The supernatants of all 12 T25 flasks were collected separately in falcons and centrifuged at 1100 rpm for 5 min at 4 °C. Next, two medium blanks were prepared: 400 µl of 100% Methanol (MeOH, HPLC LC-MS grade, VWR) spiked with four internal standards (IST; 120 pg/µl of dopamine-d4, Santa Cruz; melatonin-d4, Santa Cruz; N-acetylserotonin-d3, Toronto Research Chemical; and serotonin-d4, Santa Cruz) was added in two tubes. One of those tubes was topped-up with 100 µl of fresh RPMI to generate medium blank 1, the other one with 100 µl of the supernatant of one control T25 flask. In addition, 400 µl of MeOH + IST solution was mixed with 100 µl of the centrifuged supernatant of each of the 12 samples. To generate an extraction blank, 500 µl of MeOH + IST mixture was collected in a tube. All tubes were vortexed (Vortex-Genie® 2, Sigma-Aldrich), sealed with parafilm and immediately frozen at -20 °C.

3.6.3 Sample preparation

The samples were centrifuged with 10000×g for 2 min at room temperature (Fisherbrand™ accuSpin™ Micro 17 Microcentrifuge, Fisher Scientific). Afterwards, the entire supernatant was transferred to glass vials and dried with N_2 gas for 30 min. Meanwhile the reconstitution buffer was prepared from a mixture of 9 ml H_2O (HPLC LC-MS grade, VWR) + 1% MeOH + 0.2% formic acid (FA, Honeywell) (Table 7) mixed with 1 ml of 1:1000 dilution of caffeine-d9 standard (Table 8). After the samples were dried, 120 µl of reconstitution buffer was added to each sample. In addition, 1.5 ml of reconstitution buffer and 1.5 ml of H_2O + 1% MeOH + 0.2% FA was used as reconstitution blanks. Next, the samples were vortexed four times 3 sec each and transferred into 200 µl glass inlets which were placed into glass vials, recapped, and stored at 4 °C until measurement.

Table 7: *Composition of reconstitution buffer solvent.*

Compounds	V [µl]
H_2O	49.4
MeOH	0.5
FA	0.1

Table 8: *Composition of Caffeine-d9 standard (10 ng/µl).*

Compounds	V [µl]
H_2O	495
Caffeine-d9 (1 mg/ml, Sigma-Aldrich)	5

3.6.4 LC-MS/MS analysis

A Vanquish Ultra high-performance liquid chromatography (UHPLC) System (Thermo Fisher Scientific), equipped with a RP Kinetex XB-C18 column (100 Å, 2.6 µm, 100×2.1 mm, Phenomenex Inc.) was used for separating the analytes in the samples. Eluent A consisted of water with 0.2% FA, eluent B of MeOH with 0.2% FA. The following elution gradient flow profile was applied: 0-0.5 min at 1-5% eluent B, 0.5-5 min at 5-40% eluent B, 5-8 min at 40-90% eluent B, 5-10.5 min at 90% eluent B followed by a re-equilibration phase from 10.6-12.5 min at 1% eluent B resulting in a total run time of 12.5 min. The system was operating with a lower pressure limit of 2 bar and an upper limit of 950 bar at a flow rate of 500 µl/min. The column temperature was set to 40 °C.

Mass spectrometric analysis was conducted by a Q Exactive™ HF MS (Thermo Fisher Scientific) with an ESI source. Electrospray ionisation was performed in positive ionisation mode. An untargeted mass spectrometric approach was used to identify the compounds. All samples were analysed in technical duplicates. MS scan range from m/z 100-1000 was applied and the resolution was set to 60000 (at m/z 200) for MS^1 and 15000 (at m/z 200) for MS^2. Collision energy was set to 30 eV. Instrument control was performed using Xcalibur software (Thermo Fisher Scientifc).

3.6.5 Data analysis

The preliminary qualitative analysis was performed by the software Compound Discoverer (v.3.1.0.305, Thermo Fischer Scientific). Here the measured spectra of the positive mode only are compared to those online on mzCloud™ (08/2022) to identify metabolites present in the sample. All compounds with a match factor higher than 75 were further investigated to determine if they could be present as metabolites in the sample (true positive identifications). TraceFinder Software (v.4.1, Thermo Fischer Scientific) was then used to quantify all possible metabolites via peak integration and calculation of peak

areas. Statistical analysis was conducted via R script: areas under the curve (AUC) of all samples were log_2 transformed and normalized by subtraction of the average AUC of the two ISTs dopamine-d4 and melatonin-d4 from the sample AUC intra-sample wise. The resulting scores were summed up with 20 to obtain values typical of proteomics. Using the limma package, imputation was performed, and p values were calculated along with Benjamini-Hochberg adjusted p values. (107)

3.7 Phosphoproteomics

3.7.1 Cell treatment

At first, twelve T25 flasks were seeded with each 5 ml of cell suspension at a density of 5×10^6 cells followed by an 24 h incubation step at 37 °C and 5% CO_2. Next, the medium was replaced by treatment solutions of RPMI spiked with IC_{50} concentration of CisPt (9 µM) or RSL-3 (0.106 µM) in four bottles each. In addition, four T25 flasks were treated with RPMI alone as a control group. All flasks were incubated for 4 h at 37 °C and 5% CO_2. The treatment duration was determined in a preliminary experiment where the cellular response to either treatment at IC_{50} was visually observed for 6 h, whereupon the timepoint of 4 h was chosen.

3.7.2 Cell fraction

After 4h of incubation, the cells were washed twice with 2 ml tris-buffered saline (TBS; Table 9) and the wash was completely removed. Afterwards, 150 µl sodium deoxycholate detergent (SDC) lysis buffer (Table 10) was added to each T25 flask, cells were scraped and transferred into an Eppendorf tube. Subsequently, the suspensions were immediately heat-treated at 95 °C for 5 min. The lysates were cooled to room temperature, spun down and stored at -20 °C until further processing.

Table 9: *Composition of TBS, pH 7.4.*

Compounds	c [mM]	m [g] for 500 ml
Tris (Bio-Rad)	25	1.51
NaCl (Sigma-Aldrich)	150	4.38
H_2O	-	-
HCl (Sigma-Aldrich)	1000	-

Table 10: *Composition of SDC lysis buffer.*

Compounds	c [mM]	Percentage [%w/v]	Prepare for 10 ml
SDC (Sigma-Aldrich)	-	4	0.4 g
Tris-HCl 2M, pH 8.5	100 mM	-	500 µl
H_2O	-	-	9500 µl

3.7.3 Cell lysis

The samples were mixed at 300 rpm and 95 °C for 5 min on a thermoshaker (Eppendorf ThermoMixer®). Then, cell lysis of all samples was conducted via S220 focused-ultrasonicator (Covaris). The SonoLab software (V.7.2, Covaris) was used to adapt the method to a maximum power of 140 W, 10% duty factor and 200 cycles/burst at 15 °C for 2 min. At the end, the homogenised samples were transferred in new tubes (1.5ml, safe-lock, Eppendorf) and stored at 4 °C overnight.

3.7.4 BCA assay

A bicinchoninic acid assay (BCA) was performed to determine the protein concentration. Therefore, the samples were mixed for 5 min at 95 °C with 300 rpm on a thermoshaker. Meanwhile, calibration standards were prepared in a 96 well plate as shown in Table 11. Samples were diluted by mixing 1 µl sample with 9 µl H_2O. Immediately before use, the working reagent was prepared from 7840 µl reagent A (Table 12) with160 µl reagent B (200 mM copper sulphate pentahydrate, Sigma-Aldrich). After adding 200 µl of working reagent in each well, the plate was shaken at 1100 rpm in the dark for 1 min and then incubated at 60 °C in the dark for 30 min (drying cabinet FD 23; Binder). Finally, the absorbance was measured at a wavelength of 562 nm (Multiskan™ GO Microplate Spectrophotometer, Thermo Scientific).

Table 11: *Composition of calibration standards. BSA: Bovines serum albumin (1 µg/µl).*

Standard	V BSA [µl]	V H2O [µl]	V SDC [µl]
1	0	9	1
2	1	8	1
3	2	7	1
4	3	6	1
5	4	5	1
6	5	4	1
7	6	3	1
8	7	2	1
9	8	1	1
10	9	0	1

Table 12: *Composition of reagent A. Dissolved in 100 ml H_2O, pH 11.25.*

Compound	m [g]
Bicinchoninic acid (Sigma-Aldrich)	1
Na_2CO_3 (Carl Roth)	2
Sodium tartrate (Merck)	0.16
$NaHCO_3$ (Merck)	0.95

3.7.5 In solution protein digestion

The samples were diluted to a total of 520 µg protein in 281 µl SDC lysis buffer. Next, 31 µl of reduction/alkylation buffer (Table 13) was added to each sample and incubated at 45 °C and 1400 rpm for 5 min on a thermoshaker. Then, 200 µg of trypsin/lys-c mix (Promega) were dissolved in 200 µl trypsin buffer (Table 14) on ice. Lastly, 5.2 µl of this enzyme was added to each sample, corresponding to an enzyme to substrate ratio of 1:100. The samples were digested at 37 °C and 1400 rpm for 17 h.

Table 13: *Composition of reduction/alkylation buffer.*

Compounds	c [mM]	Prepare for stock solution	Prepare for 1 ml
Tris(2-carboxyethyl)phosphine (TCEP, Sigma-Aldrich)	100	57.4 mg in 1 ml H_2O (200 mM)	Mix 500 µl TCEP stock + 500 µl 2-CAM stock -> take 940 µl & add 60 µl 5M NaOH
2-Cloroacetamide (2-CAM, Alfa Aesar)	400	74.8 mg in 1 ml H2O (800mM)	
H_2O	-	-	
NaOH (Sigma-Aldrich)	5000	-	

Table 14: *Composition of trypsin buffer.*

Compounds	c [mM]	Percentage [% v/v]	Prepare for 10 ml
Acetic acid (Honeywell)	-	0.05	5 µl
$CaCl_2$ (Merck)	2	-	2.2 mg
H_2O	-	-	9995 µl

3.7.6 TiO_2 phosphopeptide enrichment

For the global proteome analysis, 12 µl of each sample was transferred in a new tube and stored at 4 °C until further processing. A slightly modified version of the EasyPhos (EP) workflow was used for phosphopeptide enrichment. (108)

To each remaining sample, 400 µl of isopropanol (Honeywell) was added, mixed for 30 sec at 1400 rpm and supplemented with 100 µl of EP enrichment buffer (Table 15). Then, the samples were mixed again at 1400 rpm for 30 seconds and centrifuged for 15 min at 2000×g. Afterwards, supernatants were collected in new 1,5 ml Eppendorf tubes. Titansphere TiO_2 beads (GL Sciences) were resuspended in EP loading buffer (Table 16) at a concentration of 1 mg/µl. Subsequently, 7.5 µl of suspended beads were added to each sample followed by an incubation step at 1400 rpm and 40 °C for 5 min. After the beads were pelleted by centrifugation at 2000×g for 1 min, the non-phosphopeptide supernatant was discarded. An aliquot of 1 ml EP wash buffer (Table 17) was pipetted onto each sample that were vortexed thoroughly for 30 sec and centrifuged at 2000×g for 30 sec to pellet the beads. The supernatant was discarded, and the washing procedure was repeated four times. Afterwards, the beads were resuspended in 75 µl EP transfer buffer (Table 18) and transferred to the top of a C_8-StageTip (CDS C8 Solid Empore™ Extraction Disks in pipette tips), which are placed in Eppendorf tubes for collecting the flow-through. To capture any remaining beads, the tubes were washed with another 75 µl EP transfer buffer per sample and transferred to the respective StageTip. Next, the StageTips were centrifuged at 1500×g for 8 min. After discarding the flow-through, the StageTips were placed in new Eppendorf tubes containing a glass vial inlet. Phosphopeptides were eluted into the glass inlets by adding 30 µl of EP elution buffer (Table 19) and centrifuging at 1500×g for 5 min. The procedure was repeated once more, rotating the StageTips between centrifugation steps. Finally, the samples (tubes with glass inlets) were

dried in a vacuum concentrator (miVac Duo, Genevac™) at 40 °C and stored at -20 °C until further processing.

Table 15: *Composition of EP enrichment buffer.*

Compounds	c [mM]	Percentage [% v/v]	Prepare for 100 samples
Trifluoroacetic acid (TFA, Signma Aldric)		48	4800 µl
KH_2PO_4 (Merck)	8		10.89 mg
H_2O		52	5200 µl

Table 16: *Composition of EP loading buffer.*

Compounds	Percentage [% v/v]
TFA	6
Acetonitrile (ACN, 100%, Honeywell)	80
H_2O	14

Table 17: *Composition of EP wash buffer.*

Compounds	Percentage [% v/v]
TFA	5
Isopropanol	60
H_2O	35

Table 18: *Composition of EP transfer buffer.*

Compounds	Percentage [% v/v]
TFA	0.1
Isopropanol	60.0
H_2O	39.9

Table 19: *Composition of EP elution buffer.*

Compounds	V [µl]
ACN	320.00
NH_4OH (25% w/v, Sigma-Aldrich)	178.57
H_2O	480.00

3.7.7 Peptide desalting

The samples for the global proteome analysis were constricted in a vacuum concentrator at 40 °C for 10 min. Next, the samples were resuspended with 100 µl styrenedivinylbenzene-reverse phase sulfonate (SDB-RPS) loading buffer (Table 20) and transferred to the top of SDB-RPS StageTips (SDB-RPS polymer sorbent, Fisher; in pipette tips), which are

placed in Eppendorf tubes for collecting the flow-through. Next, the StageTips were centrifuged at 1500×g for 8 min and the procedure was repeated two times (1×SDB-RPS loading buffer; 1×SDB-RPS wash buffer 2, Table 21), rotating the StageTips between centrifugation steps. After discarding the flow-through, the StageTips were placed in new Eppendorf tubes containing a glass vial inlet. The SDB-RPS elution buffer was freshly prepared as described in Table 22. Peptides were directly eluted into these glass inlets by adding 60 µl of SDB-RPS elution buffer and centrifuging at 1500×g for 5 min. Finally, the samples (tubes with glass inlet) were dried in a vacuum concentrator at 40 °C and stored at -20 °C until further processing.

Table 20: *Composition of SDB-RPS loading buffer.*

Compounds	Percentage [% v/v]
Isopropanol	99
TFA	1

Table 21: *Composition of SDB-RPS wash buffer 2.*

Compounds	Percentage [% v/v]
H_2O	94.8
ACN	5.0
TFA	0.2

Table 22: *Composition of SDB-RPS elution buffer.*

Compounds	V [µl]
H_2O	2400
ACN	1600
NH_4OH	20

3.7.8 Nano LC-MS/MS analysis

Phosphopeptides were reconstituted in 15 µl MS loading buffer containing 97.7% H_2O, 2% ACN and 0.3% TFA, ultrasonicated for 5 min at 20% power (Sonorex digital 10 P, Bandelin), centrifuged for 7 min at 15000×g and transferred into LC glass vials. Global proteome samples were reconstituted in 5 µl FA (30%) containing four standard peptides for quality control at 10 fmol/µl and diluted with 40 µl eluent A consisting of 99.9% H_2O with 0.1% FA. The reconstituted samples were ultrasonicated for 5 min at 20% power, centrifuged for 7 min at 5000×g and transferred into LC glass vials. A Dionex UltiMate™ 3000 nano system (Thermo Fisher Scientific), equipped with an Acclaim™PepMap™ C18

HPLC pre-column (2 cm × 100 µm, 100 Å, Thermo Fisher Scientific) for pre-separating the analytes in the samples. For phosphoproteome and global proteome analysis, 10 µl and 2 µl, respectively, were injected at a flow rate of 10 µl/min eluent A. After the analytes were trapped, they first were eluted at a flow rate of 300 nl/min and then separated on an Aurora series CSI UHPLC emitter column (25 cm × 75 µm, Ionopticks). Here a gradient of 8-40% eluent B consisting of 79.9% ACN with 20% H_2O and 0.1% FA was applied over 90 min.

Mass spectrometric analysis was conducted by a timsTOF™ Pro mass spectrometer (Bruker Daltonics) with a captive spray source (Bruker Daltonics). For the analyses, a data-dependent acquisition mode followed by LFQ was applied. LC-MS settings were set as described in *Seiser et al., 2021*. (109)

3.7.9 Data analysis

Data analysis was conducted by MaxQuant software (v.1.6.17.0) employing the Andromeda search engine for protein identification against the UniProt Database (version 12/2022 with 20404 entries). The search parameters were set as follows: A mass tolerance of 20 ppm and 40 ppm for MS and MS/MS spectra, respectively, a maximum of two missed cleavages per peptide and a false discovery rate (FDR) < 0.01 were allowed. Additionally, oxidation of methionine and N-terminal protein acetylation and, for phosphopeptides, phosphorylation of serine, threonine and tyrosine were selected as variable modifications. Furthermore, carbamidomethylation of cysteine was set as fixed modification. Phosphoproteomic data interpretation was performed using Perseus (version 1.6.14.0), filtering out contaminants and reverse matches. In addition, a phosphosite localization cut-off score of 0.75 (class 1) was set and a two-tailed Student's T-test was performed with an S0 value of 0.1 and an FDR cut-off of 0.05. Thus, several testing-corrected significantly regulated phosphosites were identified. Furthermore, a kinase-substrate enrichment analysis (KSEA) of class 1 phosphosites (p>0.75) was performed utilizing PhosphoSitePlus and NetworKIN. Therefore, a NetworKIN score cut-off of 2, p-value cut-off of 0.05 and substrate count cut-off of 5 was applied. Coral (web application for visualisation of qualitative and quantitative human kinome data) was used to visualize the enriched kinases in the context of the global kinome. (110–113)

4 Results and discussions

To determine how apoptosis and ferroptosis manifest at the molecular level and to discover their differences and similarities, a comprehensive workflow was applied. More specifically, biochemical assays such as AV/PI, cell viability, DCFH-DA, and mitochondrial bioenergetics analysis were used, as well as omics approaches such as metabolomics and phosphoproteomics. Here, special attention was paid to the study of cellular signalling processes using metabolites and phosphopeptides.

4.1 Biochemical assays

4.1.1 Cell viability assay

Cytotoxicity of CisPt and RSL-3 was determined by cell viability assays. Overall, CisPt and RSL-3 are both highly cytotoxic compounds, and they display potent IC_{50} values in A2780 cells. Comparison of the IC_{50} values of 24 h and 96 h incubation time showed that the values of RSL-3 are in the same order of magnitude around 100 nM. In contrast, the IC_{50} value of CisPt treatment decreased from 9 µM after 24 h incubation to 300 nM after 96 h incubation. This trend can be explained because apoptosis is a cell cycle-dependent process and thus, drugs that act via this pathway increase potency with longer incubation times. In contrast, a longer incubation period had no influence on the IC_{50} value of RSL-3, which suggests that ferroptosis induction is cell cycle independent.

Cell viability assays with 24 h incubation time showed high toxic effect in both CisPt and RSL-3 treatments, which is reflected in the low IC_{50} concentrations (Table 23). RSL-3 is more potent than CisPt in A2780 cells. This trend is also visible in the concentration effect curves (Figure 15).

Table 23: *Calculated IC_{50} values obtained by the cell viability assay at 24 h incubation time. Values are means ± standard derivations from at least three independent experiments.*

Compound	IC_{50} [µM]
CisPt	9 ± 1
RSL-3	0,106 ± 0,078

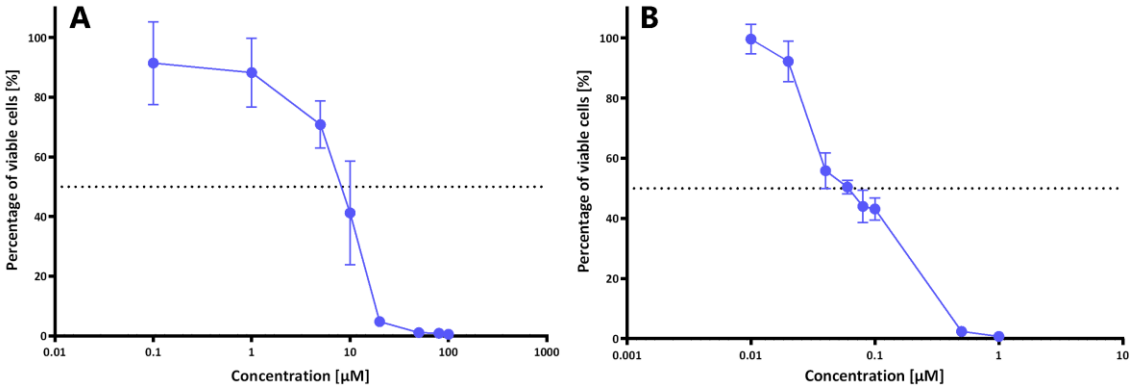

Figure 15: *Concentration-effect curves of (A) CisPt and (B) RSL-3, obtained by cell viability assay (24 h exposure). The dashed lines mark 50% inhibitory level. Values are means ± standard deviation from at least three independent experiments.*

Apoptosis and ferroptosis inhibitors were investigated to validate the respective cell death mechanisms via the viability assay. The inhibitors were added to the cell suspension before seeding. A reduction of cytotoxicity in the presence of a given inhibitor indicates a dependence of the compounds' activity on those pathways. Thus, it may be concluded that the inhibited cell death mechanism had been induced.

The 96 h treatment with CisPt showed a slightly lower IC_{50} value compared to the treatment together with 5 µM of ferrostatin-1 (Table 24, Figure 16). This may be explained by the fact that ferrostatin-1 causes iron chelation and a reduction of peroxides/radicals, which might rescue some cisplatin toxicity.

This was also reflected in the entire concentration-effect curves of CisPt-treated cells (Figure 17). In contrast, cells treated with RSL-3 and ferrostatin-1 displayed a complete inhibition of cytotoxicity, validating induction of ferroptosis as a cell death mechanism of RSL-3. (38)

Table 24: *Calculated IC_{50} values obtained by the cell viability assay at 96 h incubation time. Values are means ± standard derivations from at least three independent experiments. f1: ferrostatin-1.*

Compound	IC_{50} [nM]
CisPt	300 ± 62
CisPt + f1	476 ± 114
RSL-3	130 ± 15
RSL-3 + f1	inactive

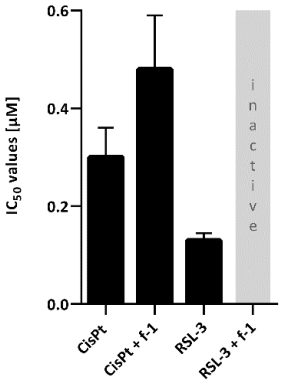

Figure 16: *Calculated IC_{50} values obtained by the cell viability assay at 96 h incubation time. Values are means ± standard derivations from at least three independent experiments. f1: ferrostatin-1.*

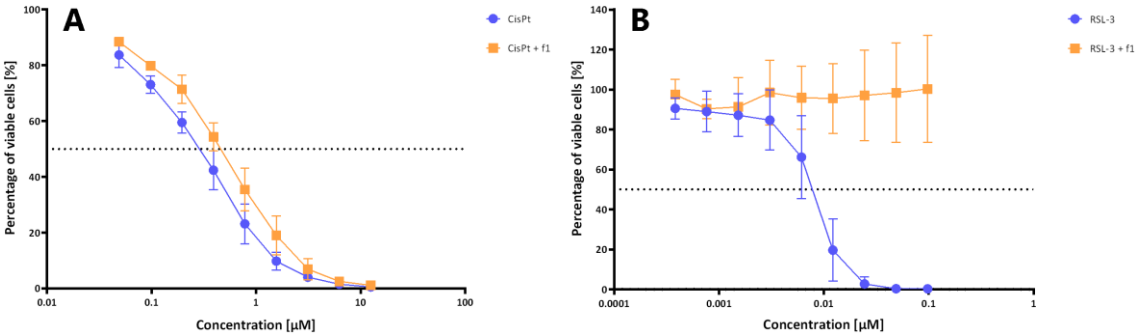

Figure 17: *Concentration-effect curves of (A) CisPt or (B) RSL-3 with and without ferrostation-1, obtained by cell viability assay (96 h exposure). The dashed lines mark the 50% inhibitory level. Values are means ± standard deviation from at least three independent experiments. f1: ferrostatin-1.*

Moreover, the 96 h treatment with CisPt together with 50 µM of the apoptosis-inhibitor AI II showed no rescuing effect compared with cells treated with CisPt alone (Figure 18). This observation contrasts with the findings of *Lademann et al.* who described in 2003 that AI II blocks the formation of the apoptosome and thus inhibits apoptosis. (27)

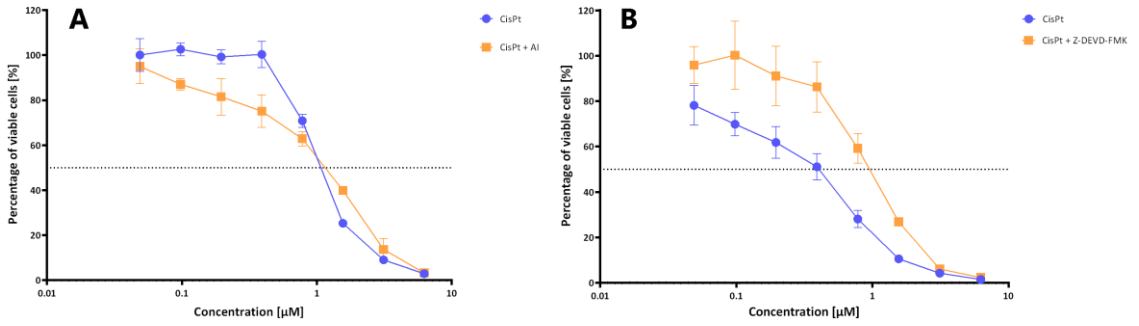

Figure 18: *Concentration-effect curves of CisPt with and without (A) AI II od (B) Z-DEVD-FMK, obtained by cell viability assay (96 h exposure). The dashed lines mark the 50% inhibitory level. Values are means ± standard deviation from one preliminary experiment.*

On the contrary, an inhibitory effect was observed for the 96 h treatment of CisPt and 20 µM of Z-DEVD-FMK, validating apoptosis as a cell death mechanism. This result is in

accordance with the current findings. In 1997, *Garcia-Calvo et al.* discovered that Z-DEVD-FMK inhibits caspase-3, thereby exerting an anti-apoptotic effect. (114)

4.1.2 AV/PI assay

A2780 cells were treated with CisPt or RSL-3 for 24 h and analysed by the flow-cytometric AV/PI assay. At least three independent experiments were averaged (Figure 19, Figure 20 and Table 25). The assay classically differentiates viable (AV-/PI-), early apoptotic (AV+/PI-), late apoptotic (AV+/PI+), and necrotic (AV-/PI+) cell fractions. Recently it was found that exposure of PS on the outer plasma membrane was not a unique characteristic of apoptotic cells and thus, non-apoptotic forms of RCD like ferroptosis can also lead to AV+ populations. (115)

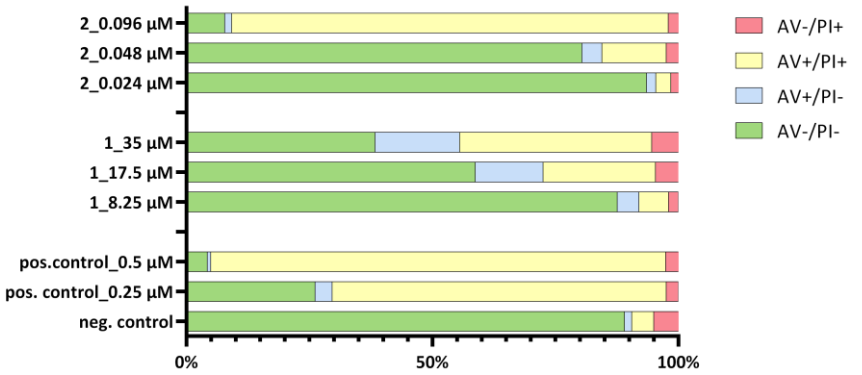

Figure 19: *Apoptosis induction by CisPt (1) and RSL-3 (2) after 24 h, analysed by the flow-cytometric AV/PI assay and averaged over at least three independent experiments differentiating viable (AV-/PI-), AV+/PI-, AV+/PI+, and necrotic (AV-/PI+) cell fractions.*

Table 25: *Apoptosis induction by CisPt and RSL-3 after 24 h, analysed by the flow-cytometric AV/PI assay differentiating viable (AV-/PI-), AV+/PI-, AV+/PI+, and necrotic (AV-/PI+) cell fractions. Results are means ± standard derivations from at least three independent experiments.*

Compound	Conc. [µM]	viable cells [%]	AV+/PI- cells [%]	AV+/PI+ cells [%]	necrotic cells [%]	∑ AV+ cells [%]
neg. control	x	89.2 ± 3.9	1.5 ± 2.6	4,5 ± 0.8	5.0 ± 5.9	6
pos. control	0.25	26.2 ± 22.5	3.5 ± 1.2	67.9 ± 24.1	2.5 ± 0.7	71
pos. control	0.50	4.2 ± 3.8	0.7 ± 0.7	92.4 ± 5.4	2.6 ± 1.0	93
CisPt	8.25	87.5 ± 4.9	4.5 ± 1.5	6.0 ± 3.4	2.0 ± 0.1	10
	17.5	58.7 ± 7.0	13.8 ± 1.6	22.8 ± 7.0	4.7 ± 1.5	37
	35	38.3 ± 3.3	17.2 ± 2.0	39.0 ± 3.2	5.4 ± 3.1	56
RSL-3	0.02	93.5 ± 1.7	1.9 ± 0.6	3.0 ± 0.8	1.6 ± 0.6	5
	0.05	80.4 ± 5.9	4.1 ± 0.6	13.1 ± 5.4	2.5 ± 0.7	17
	0.1	7.8 ± 1.4	1.4 ± 0.3	88.7 ± 2.5	2.1 ± 1.1	90

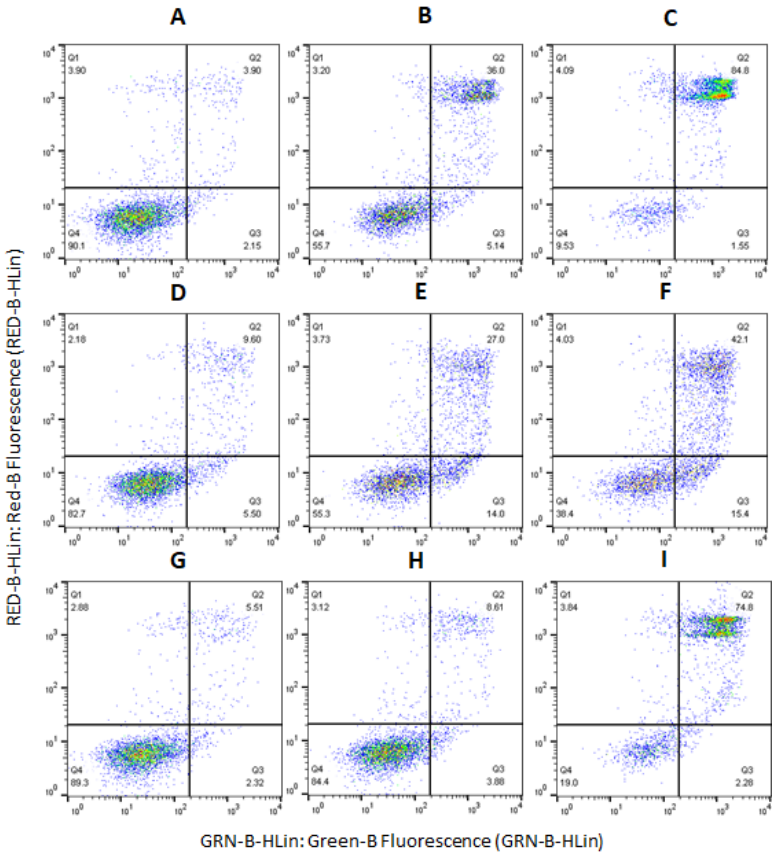

Figure 20: *Apoptosis induction by CisPt and RSL-3 after 24 h, analysed by the flow-cytometric AV/PI assay. Dot plots represent necrotic (Q1: AV–/PI+), AV+/PI+ (Q2), AV+/PI– (Q3) and viable (Q4: AV–/PI–) cell fractions (percentages indicated correspondingly) from a selected experiment: (A) untreated control, (B) positive control (0,25 µM of TM-1), (C) positive control (0,5 µM of TM-1), (D) 8,25 µM of CisPt, (E) 17,5 µM of CisPt, (F) 35 µM of CisPt, (G) 0,024 µM of RSL-3, (H) 0,048 µM of RSL-3 and (I) 0,096 µM of RSL-3.*

Cells were viable before the treatment based on the high count of viable cells of the negative control. Additionally, high amounts of apoptotic cells in the positive control indicate that the assay was performed appropriately. As expected, CisPt led to a substantial increase in cells that are described as early/late apoptotic in the assay. Moreover, a dose-dependence was observed: the higher the concentration of CisPt the more apoptotic cells were found. On the other hand, the number of necrotic cells was always minimal.

In addition, RSL-3 also induced the fraction of AV+/PI+ cells in a dose-dependent manner. The data showed that RSL-3 exhibited a stronger effect than CisPt at $2\times IC_{50}$ concentrations, which can be explained by the fact that apoptosis induction by CisPt is cell cycle dependent. Therefore, PS exposure and membrane permeabilization occur much faster

for ferroptosis compared to apoptosis. This is observable in this assay by the percentage of AV+/PI- cells that are increased upon CisPt treatment compared to RSL-3 treatment.

4.1.3 DCFH-DA assay

ROS levels were examined through DCFH-DA staining by fluorescence measurement. The measurement was started directly after the treatment with CisPt and RSL-3 (1/2×IC_{50}, IC_{50} and 2×IC_{50}) and was repeated periodically every 10 min for 2 h. Moreover, the ferroptosis inhibitor ferrostatin-1 (5 µM per well) was added to the cell suspension before seeding.

Over the course of 2 h, no substantial amount of ROS was observed upon treatment with neither cisplatin, nor RSL-3 (Figure 21). It may be worth mentioning that this fluorescent dye mainly detects soluble ROS based on peroxides or superoxide. Since the lipid peroxides formed during ferroptosis are located in the mitochondrial membrane, they may not necessarily be detected by this assay. In any case, the induction phases of apoptosis and ferroptosis do not seem to be accompanied by soluble ROS formation.

Based on the obtained data cells treated with ferrostatin-1 showed marginally decreased ROS levels in comparison to cells without inhibitor at early time points. Therefore, ferrostatin-1 seems to partially inhibit basal ROS production in the cancer cells irrespective of the treatment.

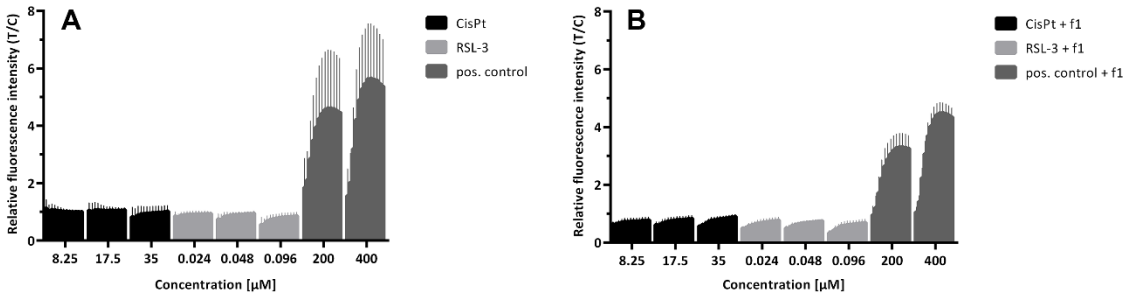

Figure 21: *ROS levels upon treatment with (A) CisPt and (B) RSL-3 with and without ferrostatin in A2780 cells obtained with the DCFH-DA assay (2 h exposure time). Values are means ± standard deviation from at least three independent experiments. Positive control: TBHP. f1: ferrostatin-1.*

4.1.4 Mitochondrial bioenergetics

The bioenergetic profile of A2780 cells treated with CisPt or RSL-3 were obtained via real-time ATP rate assay. Here, an 8-well plate with 24h pre-incubated cells was inserted into

the device followed by the 18-minute baseline measurement. Next, treatment solutions (10×IC_{50} of CisPt or RSL-3) were injected, followed by a 4-hour incubation period with hourly measurement of ECAR and OCR. OM (15 µM) was then supplemented and after three cycles of measurement, R/AA (12,5 µM) was injected and measured for three cycles.

The control group showed a distribution of mitoATP/glycoATP production rate of 37/63, while the cells treated with CisPt displayed a distribution of 44/56 (Figure 22). Therefore, the CisPt treatment caused a small change in the bioenergetic profile, resulting in more glycolysis during the induction phase of apoptosis.

In addition, the injection of OM in CisPt treatment resulted in a decrease in OCR and an increase in ECAR (Figure 23). Accordingly, the 4h treatment period was probably too short to detect major effects of apoptosis on mitochondrial uncoupling. In addition, the OM concentration could also have been too low, so that the ATP synthase was not completely inhibited and thus an overestimated mitoATP content was calculated. However, the beginning of the manifestation of the effect can be seen. (20)

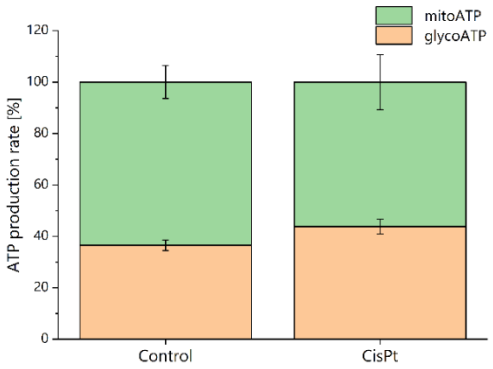

Figure 22: *Bioenergetic profile of A2780 cells with and without treatment of CisPt as the percentage ratio of mitoATP and glycoATP production rate.*

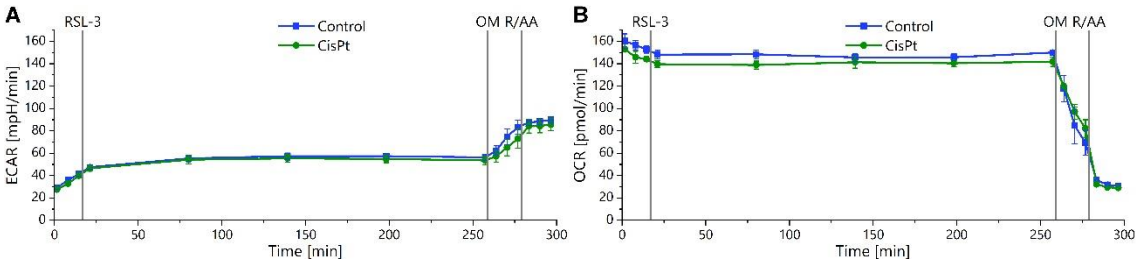

Figure 23: *(A) ECAR and (B) OCR were measured by real-time ATP rate assay when challenged by CisPt, OM, and R/AA.*

In comparison, the experiments with RSL-3 treatment showed only glycoATP production (Figure 24). As seen in Figure 25, OM injection had very little to no effect on the progression of OCR and ECAR. Consequently, no mitoATP production rate could be calculated.

In conclusion, further analyses with adapted methods need to be performed to gain better insight into the bioenergetic profile of the treated cells. Therefore, a 24 h preincubation of both CisPt and RSL-3 could be performed before measurement.

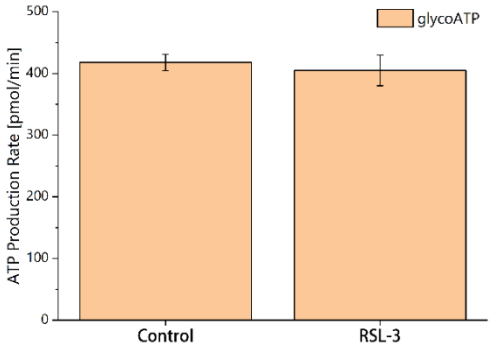

Figure 24: *Bioenergetic profile of A2780 cells with and without treatment of RSL-3.*

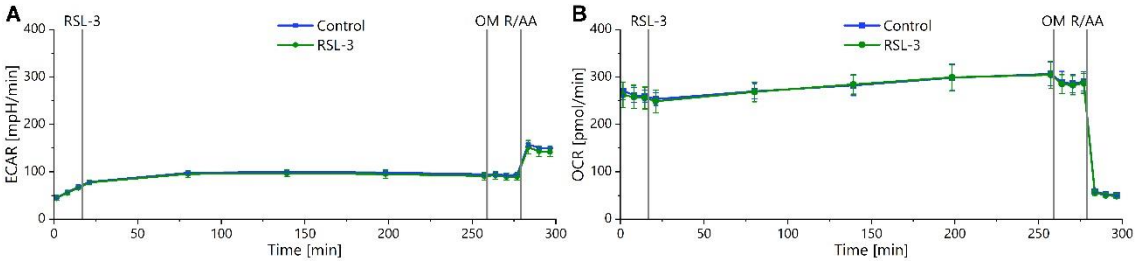

Figure 25: *(A) ECAR and (B) OCR were measured by real-time ATP rate assay when challenged by RSL-3, OM, and R/AA.*

4.2 Omics assays

4.2.1 Metabolomics

Metabolomic analysis of cell supernatants treated with IC_{50} concentrations of CisPt or RSL-3 for 4 h was performed using UHPLC Q Exactive™ HF MS. Thereby, a non-targeted approach was used as a hypothesis-generating procedure.

The Metabolomics analysis of the cell supernatant measured in positive mode revealed 93 possible metabolites with a confidence score >0.75 after comparison with Compound

Discoverer. After verification of the peaks using TraceFinder, 82 metabolites were identified and processed. A R script was developed to transform, normalize and impute the AUC values to calculate statistically significant changes, by means of p values together with Benjamini-Hochberg adjusted p values.

Figure 26 shows the distribution of the intensity (AUC) and retention time of the 82 metabolites over the course of the analysis. The metabolites were found with intensities between 16 and 30 $\log_2$(AUC)+20, with most metabolites having an average intensity of approximately 22. This amounts to a dynamic range of approximately 1E6. However, the majority of the metabolites eluted within the first 3 minutes. After that, only very few metabolites arrived until minute 12. This is reflecting poor separation using a RP column. To achieve a better result, it is necessary to improve the chromatographic separation. For this purpose, a HILIC column could be used for future experiments.

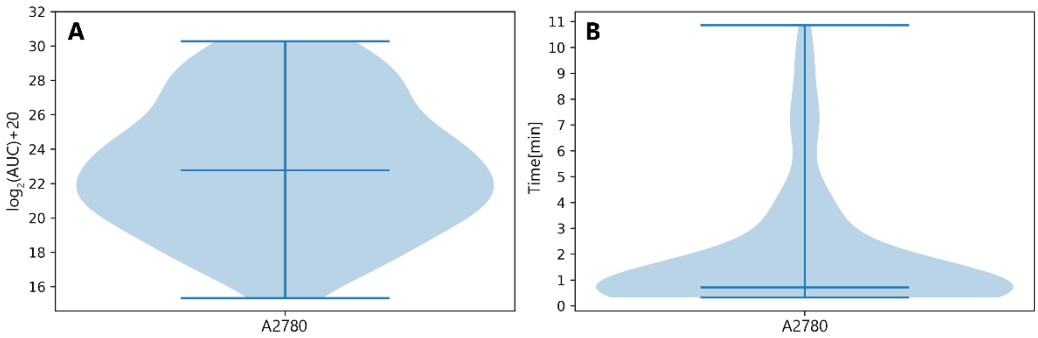

Figure 26: *Violin plot of the distribution (A) of the mean AUCs and (B) of the retention time of the metabolites. The bars show the maximum, median, and minimum of the values.*

A principal component analysis (PCA) was calculated (Figure 27). The metabolites of the blank, which consisted only of the medium, clearly distinguished from those of the cell suspensions, whether treated or not. However, no separation between treated and untreated cells is visible. In addition, the CisPt treated cells cannot be distinguished from the RSL-3 treated samples.

In addition, volcano plots were created comparing the two treatments with the control group using Benjamini-Hochberg adjusted p values. Metabolites were considered a significant hit if the adjusted p value was less than 0.05 and the $\log_2$ fold change (FC) was at least 0.5. Thus, when CisPt treated cells were compared against the control, 2 metabolites with significantly changed intensities were obtained (Figure 28A). More precisely, 4-aminobenzoic acid (PABA) is found with a reduced intensity and epinephrine with an

increased one. In comparison, 3 metabolites with significantly increased intensities (4-aminophenol, anthranillic acid, epinephrine) and 2 metabolites with significantly decreased intensities (acetyllysine, glycylleucine) were found in RSL-3 treated cells compared to control (Figure 28B).

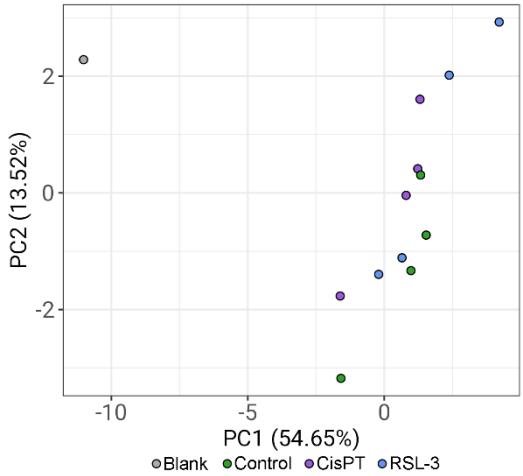

Figure 27: *PCA of the metabolites of the cell supernatant.*

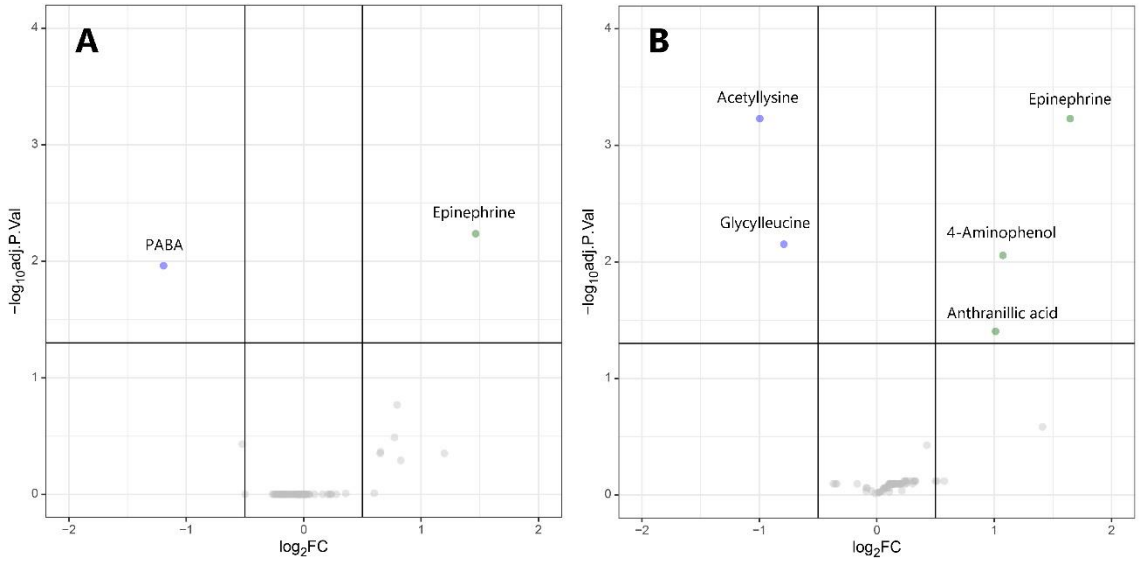

Figure 28: *Volcano plots of the metabolites found in the supernatant of treated A2780 cells identified by MS. (A) CisPt treatment vs control; (B) RSL-3 treatment vs control; X-axis: log_2 of FC. Y-axis: -log_{10} of adjusted p values; coloured dots: metabolites with a significant hit; horizontal line: p value = 0.05; vertical line: FC of ± 0.5.*

Intensities of epinephrine, a known marker of stress, were increased in both treatments compared with the control group (Figure 29B). (116)

Anthranilic acid had the lowest AUCs in the control group, followed by the CisPt treated cells and the highest intensities were shown by the cells with RSL-3 treatment (Figure 29A). The metabolite has an antioxidant effect and inhibits the Fenton reaction, which

plays an important role in ferroptosis. Since apoptosis can also be induced by ROS, anthranilic acid has inhibitory effects for both cell death mechanisms. (117)

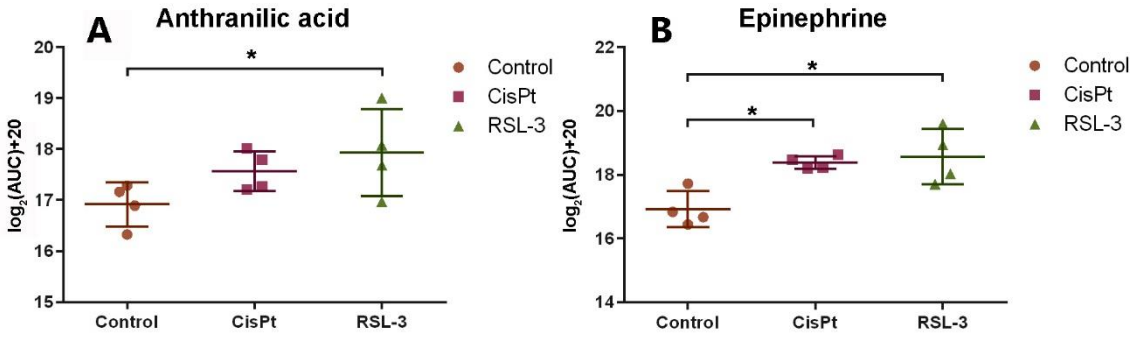

Figure 29: *Levels of (A) anthranilic acid and (B) epinephrine in A2780 cells either untreated or treated with CisPt or RSL-3. (*) significantly regulated.*

The two metabolites acetyllysines and glycylleucines showed the same trend: The control group had the highest intensities, followed by the CisPt-treated cells, and the cells with RSL-3 treatment had the lowest AUCs (Figure 30). Thus, the two amino acids were consumed by RSL-3 treated cells. Overall, glycylleucine consistently displayed slightly higher levels than acetyllysine.

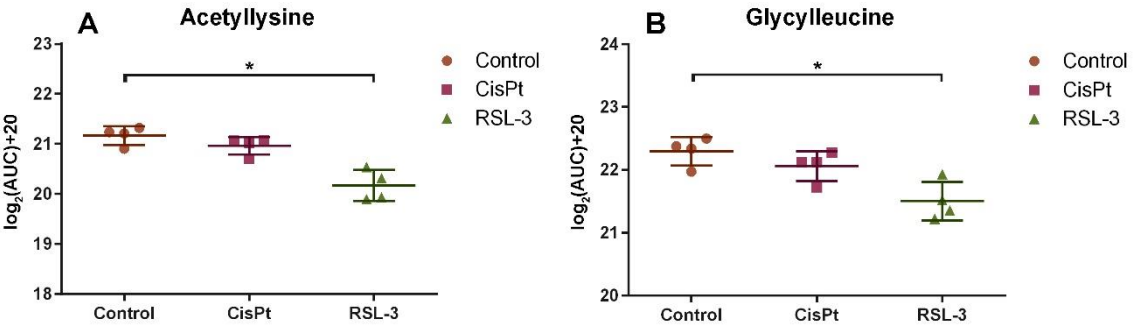

Figure 30: *Levels of (A) acetylglycine and (B) glycylleucine in A2780 cells either untreated or treated with CisPt or RSL-3. (*) significantly regulated.*

Levels of 4-aminophenol were enhanced in both treatments in comparison with the control group, being highest in the group with RSL-3 treatment (Figure 31A). 4-Aminophenol is a degradation product of PABA. It is known that photoactivation of PABA leads to this metabolite, among others. In addition, the enzyme 4-aminobenzoate hydroxylase converts PABA to 4-aminophenol. So far, this has only been described in agaricus bisporus, but this or a similar enzyme may also occur in humans, which has not yet been characterised. (118, 119)

PABA was not detected in the blank sample or in the cells treated with CisPt. However, the metabolite was found in the supernatant of the control group and of the RSL-3 treated cells (Figure 31B). Thus, PABA seemed to be naturally excreted by cells. So, if cells were treated with CisPt, excretion was apparently prevented or occurred only in a very small amount and the metabolite was apparently downregulated. Since CisPt is known for its ability to block transporters, especially copper carriers, it may also block the one for PABA. (120)

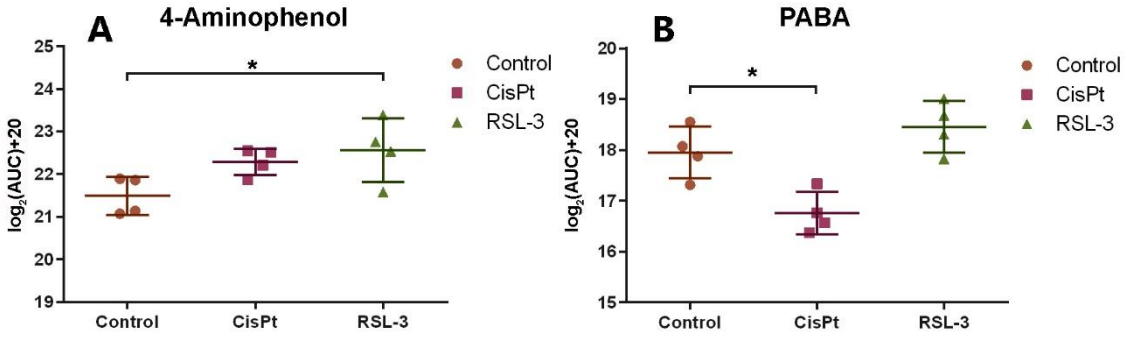

Figure 31: *Levels of (A) 4-aminophenol and (B) PABA in A2780 cells either untreated or treated with CisPt or RSL-3. (*) significantly regulated.*

4.2.2 Phosphoproteomics

Phosphoproteomic analysis of whole cell lysates treated with IC_{50} concentrations of CisPt or RSL-3 for 4 h was conducted via timsTOF™ Pro MS. Here, an LFQ approach was used to determine enriched kinases that may provide insight into the biomolecular mechanism of the two cell death mechanisms. Kinases can be identified based on their phosphorylation of proteins using the identified phosphopeptides.

The phosphoproteomic analysis leaded to the identification of a total of 4,518 phosphosites. These phosphopeptides were used to perform a kinase substrate enrichment analysis (Figure 32). As a result, 219 kinases were found in both treatments to be potentially responsible for the regulations of the observe phosphopeptides. Furthermore, the analysis showed that the activity of 15 kinases was significantly increased and 10 decreased in the CisPt treatment compared to the control. Upon treatment with RSL-3, the activity of 10 kinases was found significantly increased and 5 decreased. Increased activities of 4 kinases were found after both treatments: *BCKDK*, *ICK*, *mTOR*, *PDK1*. In contrast, the activity of the 2 kinases (*AURKB*, *Nek2*) was decreased after both treatments. In addition,

treatment with CisPt resulted in a wider range of z-score, which indicates the extent to which a given value deviates from the mean value. Consequently, CisPt treatment led to a slightly stronger effect on kinases compared to the control group than RSL-3 treatment.

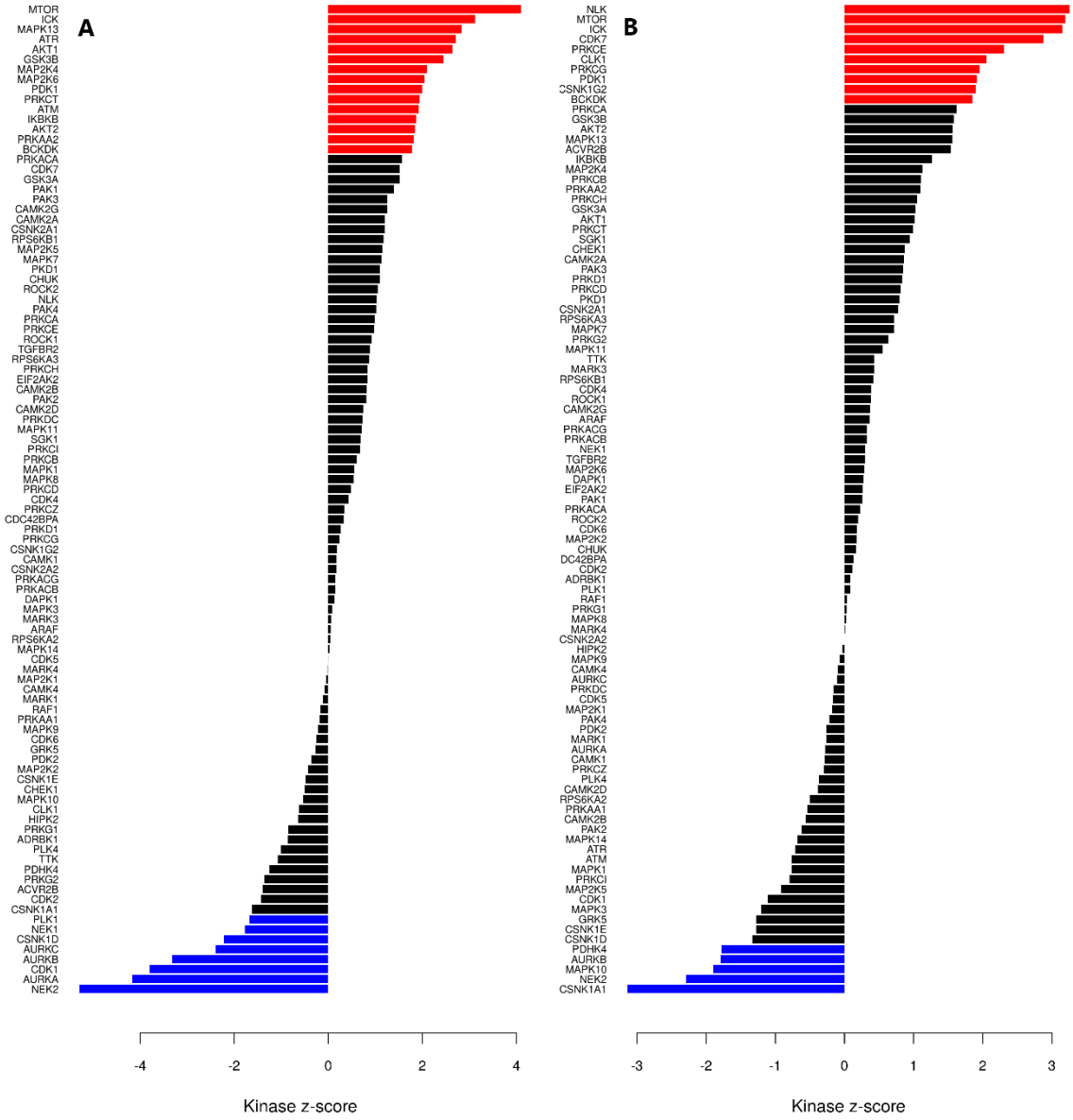

Figure 32: *KSEA waterfall plots showing significantly enriched (red) and de-enriched kinases (blue) after exposure of (A) CisPt and (B) RSL-3 to A2780 cells.*

Additionally, kinome trees were generated for both treatments using Coral, potentially mapping 522 kinases. (Figure 33, Figure 34). For this purpose, the z-values and substrate counts calculated by KSEA were provided to Coral. Here the red branches and nodes reflect increased and blue decreased kinase activities.

As already shown by KSEA, the kinases *BCKDAK*, *mTOR* and *PDK1* were enhanced in both treatments. The kinases all have in common that they regulate cellular metabolism. Consequently, with both CisPt and RSL-3 treatment, cellular metabolism was activated. (121–123)

Furthermore, in both cases the activity of tyrosine kinases (*TK*) was mostly reduced. Only the TK, *Src*, was enhanced, which among other roles controls cell cycle progression and acts as an inhibitor of the mitochondrial pathway of apoptosis. Therefore, the upregulation of the kinase may indicate that cell death processes had already been initiated in the cells. In addition, the coherently decreased activity of *TK* after CisPt or RSL-3 treatment might be associated with phosphatidylserine exposure, as evidenced in the AV/PI assay. (124, 125)

Both treatments caused the strongest reduced activity of the kinases *AurA*, *CDK1*, *Nek2*, which all control the cell cycle. Consequently, mitotic cell cycle activity was downregulated in both treatments. (126)

Furthermore, treatment with CisPt led to an enhanced activity of the *AGC* and *CAM* kinase families. In contrast, treatment with RSL-3 showed a reduced activity of those kinase families. However, only *Akt* and *PKC* of the AGC family remained upregulated. *PKC* is implicated in both apoptosis and ferroptosis induction, while *Akt* regulates cellular survival pathways, thereby suppressing cell death mechanisms. Since the cells were only exposed to a 4 h treatment, cell fate may not have been decided yet. (127–130)

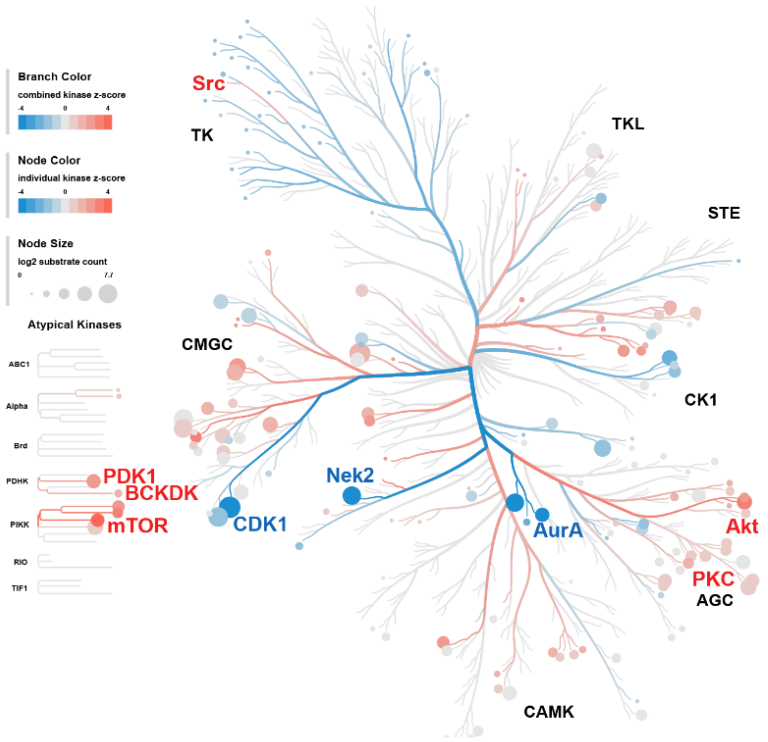

Figure 33: *CisPt induced kinome activation in A2780 cells. Red indicates an increased and blue a decreased activity of kinases.*

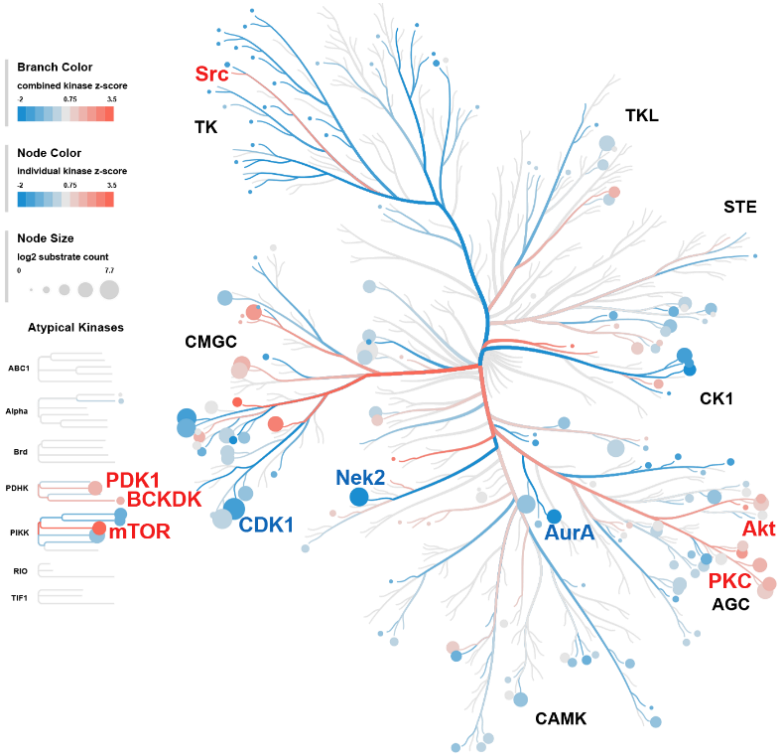

Figure 34: *RSL-3 induced kinome activation in A2780 cells. Red indicates an increased and blue a decreased activity of kinases.*

5 Conclusion and outlook

This master thesis investigated apoptosis and ferroptosis pathways in detail on the molecular level. In contrast to apoptosis, which is mediated by caspase activation, the mechanisms of ferroptosis are not elucidated in detail. To fill this gap an extensive experimental design was carried out involving both traditional biochemical tests (AV/PI assay, cell viability assay, DCFH-DA assay, mitochondrial bioenergetics analysis) and comprehensive multi-omics analyses (non-targeted metabolomics, LFQ phosphoproteomics).

Cell viability assays determined cytotoxicity of CisPt and RSL-3 in A2780 cells. Longer CisPt treatments led to increased toxicity, whereas RSL-3 treatment showed no potency change by increasing incubation times. The caspase-3 inhibitor Z-DEVD-FMK exhibited a small apoptosis inhibitory effect upon CisPt treatment. On the contrary, a massive ferroptosis inhibition was observed for RSL-3 treatments in the presence of the ferroptosis inhibitor ferrostatin-1.

Flow-cytometric analysis of A2780 cells showed that PS release and membrane permeabilization occurred after induction of both cell death pathways. Apoptosis was characterized by a significant population of cells that lacked membrane permeabilization and exposure of phosphatidylserine, whereas RSL-3-induced ferroptosis showed a minimal proportion of those cells.

DCFH-DA staining showed that both CisPt and RSL-3 treatments did not induce a significant amount of ROS over the course of 2 h. Thus, the induction of these cell death pathways is not associated with soluble ROS. Yet, basal ROS production in cancer cells was partially inhibited by ferrostatin-1 independent of treatment.

However, the examination of mitochondrial bioenergetics was inconclusive after 4 hours of treatment with CisPt and RSL-3. CisPt treatment showed no apparent change. Therefore, these experiments need to be repeated with a 24 h pre-incubation of both CisPt and RSL-3 prior to measurement.

Additionally, metabolomics analysis of the cell supernatant after 4 h of treatment with CisPt and RSL-3 revealed 82 metabolites of interest, 6 of which showed significantly different intensities depending on the treatment. Both similarities and differences of the

two cell death mechanisms in the metabolic profile were successfully detected. Epinephrine, a stress marker, showed increased levels with both CisPt and RSL-3 treatment compared to the control group. The two metabolites acetyllysine and glycylleucine were consumed more strongly upon RSL-3 treatment. In comparison, the release of PABA was inhibited upon CisPt treatment, but was found in both the control group and cells treated with RSL-3. It would be interesting to analyse secreted lipid mediators.

Furthermore, phosphoproteomics of cells treated with CisPt or RSL-3 for 4 h enabled the identification of cellular signalling processes during the induction of apoptosis and ferroptosis. A total of 4,518 phosphosites were identified that were attributable to 219 kinases after kinase substrate enrichment analysis. One common feature was that the generally reduced activity of tyrosine kinases, except for the kinase *Src*., which regulates cell cycle progression. A major contrast of the two treatments was found in the enrichment of the kinase families *CAM* and *AGC*. These were upregulated in CisPt treatment but downregulated in RSL-3 treatment except for the two kinases *Act* and *PKC*. Since *PKC* seems to induce both apoptosis and ferroptosis, whereas Akt suppresses cell death mechanisms, the fate of cells may not yet be decided after 4 h treatment.

In summary, analysis of traditional biochemical assays showed subtile differences between apoptosis and ferroptosis. In contrast, metabolomics and phosphoproteomics analyses revealed not only some similarities but also clear differences between the two cell death mechanisms. The newly acquired knowledge plus further investigations help to achieve a better understanding of the underlying mechanisms of the cell death mechanisms of apoptosis and ferroptosis. This insight may be used in drug discovery programs to identify ferroptosis-inducing agents based on molecular signatures.

References

(1) Galluzzi, L., et al., Molecular mechanisms of cell death: recommendations of the Nomenclature Committee on Cell Death 2018*, Cell Death and Differentiation*, **2018***, 25,* 486–541. doi: 10.1038/s41418-017-0012-4.

(2) Kroemer, G., et al., Classification of cell death: recommendations of the Nomenclature Committee on Cell Death 2009*, Cell Death and Differentiation*, **2009***, 16,* 3–11. doi: 10.1038/cdd.2008.150.

(3) Christofferson, D.E.; Yuan, J., Necroptosis as an alternative form of programmed cell death*, Current Opinion in Cell Biology*, **2010***, 22,* 263–268. doi: 10.1016/j.ceb.2009.12.003.

(4) Guo, J., et al., Ferroptosis: A Novel Anti-tumor Action for Cisplatin*, Cancer Research and Treatment*, **2018***, 50,* 445–460. doi: 10.4143/crt.2016.572.

(5) Galanski, M., Recent developments in the field of anticancer platinum complexes*, Recent Patents on Anti-Cancer Drug Discovery*, **2006***, 1,* 285–295. doi: 10.2174/157489206777442287.

(6) Shen, D.-W.; Pouliot, L.M.; Hall, M.D.; Gottesman, M.M., Cisplatin resistance: a cellular self-defense mechanism resulting from multiple epigenetic and genetic changes*, Pharmacological Reviews*, **2012***, 64,* 706–721. doi: 10.1124/pr.111.005637.

(7) Li, J., et al., Ferroptosis: past, present and future*, Cell Death & Disease*, **2020***, 11,* 88. doi: 10.1038/s41419-020-2298-2.

(8) Jiang, X.; Stockwell, B.R.; Conrad, M., Ferroptosis: mechanisms, biology and role in disease*, Nature Reviews Molecular Cell Biology*, **2021***, 22,* 266–282. doi: 10.1038/s41580-020-00324-8.

(9) Bruno, P.M., et al., A subset of platinum-containing chemotherapeutic agents kills cells by inducing ribosome biogenesis stress*, Nature Medicine*, **2017***, 23,* 461–471. doi: 10.1038/nm.4291.

(10) Hangauer, M.J., et al., Drug-tolerant persister cancer cells are vulnerable to GPX4 inhibition*, Nature*, **2017***, 551,* 247–250. doi: 10.1038/nature24297.

(11) Viswanathan, V.S., et al., Dependency of a therapy-resistant state of cancer cells on a lipid peroxidase pathway*, Nature*, **2017***, 547,* 453–457. doi: 10.1038/nature23007.

(12) Tomasetti, C.; Li, L.; Vogelstein, B., Stem cell divisions, somatic mutations, cancer etiology, and cancer prevention*, Science*, **2017***, 355,* 1330–1334. doi: 10.1126/science.aaf9011.

(13) Muro-Cacho, C.A., *Carcinogenesis,* Wiley. Hoboken, NJ, **2015**.

(14) Hanahan, D., Hallmarks of Cancer: New Dimensions*, Cancer Discovery*, **2022***, 12,* 31–46. doi: 10.1158/2159-8290.CD-21-1059.

(15) Hanahan, D.; Weinberg, R.A., Hallmarks of cancer: the next generation*, Cell*, **2011***, 144,* 646–674. doi: 10.1016/j.cell.2011.02.013.

(16) Evan, G.I.; Vousden, K.H., Proliferation, cell cycle and apoptosis in cancer*, Nature*, **2001***, 411,* 342–348. doi: 10.1038/35077213.

(17) Siddiqui, I.A.; Sanna, V.; Ahmad, N.; Sechi, M.; Mukhtar, H., Resveratrol nanoformulation for cancer prevention and therapy*, Annals of the New York Academy of Sciences*, **2015***, 1348,* 20–31. doi: 10.1111/nyas.12811.

(18) Grimm, S., Die Apoptose: Programmierter Zelltod*, Chemie in unserer Zeit*, **2003***, 37,* 172–178. doi: 10.1002/ciuz.200300260.

(19) Elmore, S., Apoptosis: a review of programmed cell death, *Toxicologic Pathology*, **2007**, *35,* 495–516. doi: 10.1080/01926230701320337.
(20) Brown, D.A.; Yang, N.; Ray, S.D., *Apoptosis,* Academic Press. Cambridge, MA, **2014**.
(21) Savill, J.; Fadok, V., Corpse clearance defines the meaning of cell death, *Nature*, **2000**, *407,* 784–788. doi: 10.1038/35037722.
(22) Renehan, A.G.; Booth, C.; Potten, C.S., What is apoptosis, and why is it important?, *British Medical Journal*, **2001**, *322,* 1536–1538. doi: 10.1136/bmj.322.7301.1536.
(23) Taylor, R.C.; Cullen, S.P.; Martin, S.J., Apoptosis: controlled demolition at the cellular level, *Nature Reviews Molecular Cell Biology*, **2008**, *9,* 231–241. doi: 10.1038/nrm2312.
(24) Strasser, A.; O'Connor, L.; Dixit, V.M., Apoptosis signaling, *Annual Review of Biochemistry*, **2000**, *69,* 217–245. doi: 10.1146/annurev.biochem.69.1.217.
(25) Susin, S.A., et al., Two distinct pathways leading to nuclear apoptosis, *The Journal of Experimental Medicine*, **2000**, *192,* 571–580. doi: 10.1084/jem.192.4.571.
(26) SMART - Servier Medical ART. https://smart.servier.com/, (Accessed March 6, 2023).
(27) Lademann, U., et al., Diarylurea compounds inhibit caspase activation by preventing the formation of the active 700-kilodalton apoptosome complex, *Molecular and Cellular Biology*, **2003**, *23,* 7829–7837. doi: 10.1128/MCB.23.21.7829-7837.2003.
(28) Lee, J.; Bogyo, M., Development of near-infrared fluorophore (NIRF)-labeled activity-based probes for in vivo imaging of legumain, *ACS Chemical Biology*, **2010**, *5,* 233–243. doi: 10.1021/cb900232a.
(29) Patel, R.P., et al., Cross-resistance of cisplatin selected cells to anti-microtubule agents: Role of general survival mechanisms, *Translational Oncology*, **2021**, *14,* 100917. doi: 10.1016/j.tranon.2020.100917.
(30) Cepeda, V., et al., Biochemical mechanisms of cisplatin cytotoxicity, *Anti-Cancer Agents in Medicinal Chemistry*, **2007**, *7,* 3–18. doi: 10.2174/187152007779314044.
(31) Galluzzi, L., et al., Molecular mechanisms of cisplatin resistance, *Oncogene*, **2012**, *31,* 1869–1883. doi: 10.1038/onc.2011.384.
(32) Ott, I.; Gust, R., Besonderheiten anorganischer Zytostatika. Medizinische Chemie der Platinkomplexe, *Pharmazie in unserer Zeit*, **2006**, *35,* 124–133. doi: 10.1002/pauz.200500161.
(33) Galluzzi, L., et al., Systems biology of cisplatin resistance: past, present and future, *Cell Death & Disease*, **2014**, *5,* e1257. doi: 10.1038/cddis.2013.428.
(34) Dixon, S.J., et al., Ferroptosis: an iron-dependent form of nonapoptotic cell death, *Cell*, **2012**, *149,* 1060–1072. doi: 10.1016/j.cell.2012.03.042.
(35) Guan, Q.; Zhou, L.-L.; Dong, Y.-B., Ferroptosis in cancer therapeutics: a materials chemistry perspective, *Journal of Materials Chemistry B*, **2021**, *9,* 8906–8936. doi: 10.1039/d1tb01654g.
(36) Liang, C.; Zhang, X.; Yang, M.; Dong, X., Recent Progress in Ferroptosis Inducers for Cancer Therapy, *Advanced Materials*, **2019**, *31,* e1904197. doi: 10.1002/adma.201904197.
(37) Sui, X., et al., RSL3 Drives Ferroptosis Through GPX4 Inactivation and ROS Production in Colorectal Cancer, *Frontiers in Pharmacology*, **2018**, *9,* 1371. doi: 10.3389/fphar.2018.01371.
(38) Miotto, G., et al., Insight into the mechanism of ferroptosis inhibition by ferrostatin-1, *Redox Biology*, **2020**, *28,* 101328. doi: 10.1016/j.redox.2019.101328.

(39) Yang, W.S.; Stockwell, B.R., Synthetic lethal screening identifies compounds activating iron-dependent, nonapoptotic cell death in oncogenic-RAS-harboring cancer cells*, Chemistry & Biology*, **2008***, 15,* 234–245. doi: 10.1016/j.chembiol.2008.02.010.
(40) Vigil, D.; Cherfils, J.; Rossman, K.L.; Der, C.J., Ras superfamily GEFs and GAPs: validated and tractable targets for cancer therapy?*, Nature Reviews Cancer*, **2010***, 10,* 842–857. doi: 10.1038/nrc2960.
(41) Shintoku, R., et al., Lipoxygenase-mediated generation of lipid peroxides enhances ferroptosis induced by erastin and RSL3*, Cancer Science*, **2017***, 108,* 2187–2194. doi: 10.1111/cas.13380.
(42) Liu, H., et al., Small-molecule allosteric inhibitors of GPX4*, Cell Chemical Biology*, **2022***, 29,* 1680-1693.e9. doi: 10.1016/j.chembiol.2022.11.003.
(43) Rieger, A.M.; Nelson, K.L.; Konowalchuk, J.D.; Barreda, D.R., Modified annexin V/propidium iodide apoptosis assay for accurate assessment of cell death*, Journal of Visualized Experiments*, **2011**. doi: 10.3791/2597.
(44) Balaji, N., et al., Annexin v - affinity assay - apoptosis detection system in granular cell ameloblastoma*, Journal of International Oral Health*, **2013***, 5,* 25–30.
(45) Kupcho, K., et al., A real-time, bioluminescent annexin V assay for the assessment of apoptosis*, Apoptosis*, **2019***, 24,* 184–197. doi: 10.1007/s10495-018-1502-7.
(46) Koopman, G., et al., Annexin V for flow cytometric detection of phosphatidylserine expression on B cells undergoing apoptosis*, Blood*, **1994***, 84,* 1415–1420.
(47) Concha, N.O.; Head, J.F.; Kaetzel, M.A.; Dedman, J.R.; Seaton, B.A., Annexin V forms calcium-dependent trimeric units on phospholipid vesicles*, FEBS Letters*, **1992***, 314,* 159–162. doi: 10.1016/0014-5793(92)80964-I.
(48) Rieger, A.M.; Hall, B.E.; Le Luong, T.; Schang, L.M.; Barreda, D.R., Conventional apoptosis assays using propidium iodide generate a significant number of false positives that prevent accurate assessment of cell death*, Journal of Immunological Methods*, **2010***, 358,* 81–92. doi: 10.1016/j.jim.2010.03.019.
(49) Vermes, I.; Haanen, C.; Reutelingsperger, C., Flow cytometry of apoptotic cell death*, Journal of Immunological Methods*, **2000***, 243,* 167–190. doi: 10.1016/S0022-1759(00)00233-7.
(50) Grela, E.; Kozłowska, J.; Grabowiecka, A., Current methodology of MTT assay in bacteria - A review*, Acta Histochemica*, **2018***, 120,* 303–311. doi: 10.1016/j.acthis.2018.03.007.
(51) Ho, W.Y.; Yeap, S.K.; Ho, C.L.; Rahim, R.A.; Alitheen, N.B., Development of multicellular tumor spheroid (MCTS) culture from breast cancer cell and a high throughput screening method using the MTT assay*, PloS One*, **2012***, 7,* e44640. doi: 10.1371/journal.pone.0044640.
(52) Scherliess, R., The MTT assay as tool to evaluate and compare excipient toxicity in vitro on respiratory epithelial cells*, International Journal of Pharmaceutics*, **2011***, 411,* 98–105. doi: 10.1016/j.ijpharm.2011.03.053.
(53) Price, P.; McMillan, T.J., Use of the Tetrazolium Assay in Measuring the Response of Human Tumor Cells to Ionizing Radiation*, Cancer Research*, **1990***, 50,* 1392–1396.
(54) Aranda, A., et al., Dichloro-dihydro-fluorescein diacetate (DCFH-DA) assay: a quantitative method for oxidative stress assessment of nanoparticle-treated cells*, Toxicology in Vitro*, **2013***, 27,* 954–963. doi: 10.1016/j.tiv.2013.01.016.
(55) Amer, J.; Goldfarb, A.; Fibach, E., Flow cytometric measurement of reactive oxygen species production by normal and thalassaemic red blood cells*, European Journal of Haematology*, **2003***, 70,* 84–90. doi: 10.1034/j.1600-0609.2003.00011.x.

(56) Serpa, P.B.S.; Woolcock, A.; Taylor, S.D.; Pires Dos Santos, A., Validation of a flow cytometric assay to detect intraerythrocytic reactive oxygen species in horses*, Veterinary Clinical Pathology*, **2021***, 50,* 20–27. doi: 10.1111/vcp.12976.
(57) Bond, S.T.; McEwen, K.A.; Yoganantharajah, P.; Gibert, Y., Live Metabolic Profile Analysis of Zebrafish Embryos Using a Seahorse XF 24 Extracellular Flux Analyzer*, Methods in Molecular Biology*, **2018***, 1797,* 393–401. doi: 10.1007/978-1-4939-7883-0_21.
(58) Wettmarshausen, J.; Perocchi, F., Assessing Calcium-Stimulated Mitochondrial Bioenergetics Using the Seahorse XF96 Analyzer*, Methods in Molecular Biology*, **2019***, 1925,* 197–222. doi: 10.1007/978-1-4939-9018-4_18.
(59) Caines, J.K.; Barnes, D.A.; Berry, M.D., The Use of Seahorse XF Assays to Interrogate Real-Time Energy Metabolism in Cancer Cell Lines*, Methods in Molecular Biology*, **2022***, 2508,* 225–234. doi: 10.1007/978-1-0716-2376-3_17.
(60) Horgan, R.P.; Kenny, L.C., 'Omic' technologies: genomics, transcriptomics, proteomics and metabolomics*, The Obstetrician & Gynaecologist*, **2011***, 13,* 189–195. doi: 10.1576/toag.13.3.189.27672.
(61) Ulrich-Merzenich, G., et al., Application of the "-Omic-" technologies in phytomedicine*, Phytomedicine*, **2007***, 14,* 70–82. doi: 10.1016/j.phymed.2006.11.011.
(62) Karimi, M.R.; Karimi, A.H.; Abolmaali, S.; Sadeghi, M.; Schmitz, U., Prospects and challenges of cancer systems medicine: from genes to disease networks*, Briefings in Bioinformatics*, **2022***, 23*. doi: 10.1093/bib/bbab343.
(63) AlphaFold Protein Structure Database. https://alphafold.ebi.ac.uk/, (Accessed February 9, 2023).
(64) Martins-de-Souza, D., *Shotgun proteomics: Methods and protocols,* Humana Press. Totowa, NJ, **2014**.
(65) Liu, Y.; Hüttenhain, R.; Collins, B.; Aebersold, R., Mass spectrometric protein maps for biomarker discovery and clinical research*, Expert Review of Molecular Diagnostics*, **2013***, 13,* 811–825. doi: 10.1586/14737159.2013.845089.
(66) UniProt Consortium. UniProt: a worldwide hub of protein knowledge*, Nucleic Acids Research*, **2019***, 47,* D506-D515. doi: 10.1093/nar/gky1049.
(67) Mirza, S.P.; Olivier, M., Methods and approaches for the comprehensive characterization and quantification of cellular proteomes using mass spectrometry*, Physiological Genomics*, **2008***, 33,* 3–11. doi: 10.1152/physiolgenomics.00292.2007.
(68) Bubis, J.A.; Levitsky, L.I.; Ivanov, M.V.; Tarasova, I.A.; Gorshkov, M.V., Comparative evaluation of label-free quantification methods for shotgun proteomics*, Rapid Communications in Mass Spectrometry*, **2017***, 31,* 606–612. doi: 10.1002/rcm.7829.
(69) Sobsey, C.A., et al., Targeted and Untargeted Proteomics Approaches in Biomarker Development*, Proteomics*, **2020***, 20,* e1900029. doi: 10.1002/pmic.201900029.
(70) Tang, J.; Gao, M.; Deng, C.; Zhang, X., Recent development of multi-dimensional chromatography strategies in proteome research*, Journal of Chromatography B*, **2008***, 866,* 123–132. doi: 10.1016/j.jchromb.2008.01.029.
(71) Aebersold, R.; Mann, M., Mass spectrometry-based proteomics*, Nature*, **2003***, 422,* 198–207. doi: 10.1038/nature01511.
(72) Meier-Menches, S.M., et al., An Organometallic Gold(I) Bis-N-Heterocyclic Carbene Complex with Multimodal Activity in Ovarian Cancer Cells*, Chemistry*, **2020***, 26,* 15528–15537. doi: 10.1002/chem.202003495.
(73) Skos, L.; Borutzki, Y.; Gerner, C.; Meier-Menches, S.M., Methods to identify protein targets of metal-based drugs*, Current Opinion in Chemical Biology*, **2023***, 73,* 102257. doi: 10.1016/j.cbpa.2022.102257.

(74) Meier, S.M., et al., An Organoruthenium Anticancer Agent Shows Unexpected Target Selectivity For Plectin*, Angewandte Chemie*, **2017***, 56,* 8267–8271. doi: 10.1002/anie.201702242.
(75) Arrington, J.V.; Hsu, C.-C.; Elder, S.G.; Andy Tao, W., Recent advances in phosphoproteomics and application to neurological diseases*, The Analyst*, **2017***, 142,* 4373–4387. doi: 10.1039/c7an00985b.
(76) Solari, F.A.; Dell'Aica, M.; Sickmann, A.; Zahedi, R.P., Why phosphoproteomics is still a challenge*, Molecular BioSystems*, **2015***, 11,* 1487–1493. doi: 10.1039/c5mb00024f.
(77) Needham, E.J.; Parker, B.L.; Burykin, T.; James, D.E.; Humphrey, S.J., Illuminating the dark phosphoproteome*, Science Signaling*, **2019***, 12*. doi: 10.1126/scisignal.aau8645.
(78) Bhullar, K.S., et al., Kinase-targeted cancer therapies: progress, challenges and future directions*, Molecular Cancer*, **2018***, 17,* 48. doi: 10.1186/s12943-018-0804-2.
(79) Mueller, B.K.; Mack, H.; Teusch, N., Rho kinase, a promising drug target for neurological disorders*, Nature Reviews Drug Discovery*, **2005***, 4,* 387–398. doi: 10.1038/nrd1719.
(80) Sacco, F., et al., Phosphoproteomics Reveals the GSK3-PDX1 Axis as a Key Pathogenic Signaling Node in Diabetic Islets, *Cell Metabolism*, **2018**, *6*, 1422-1432. doi: 10.1016/ j.cmet.2019.02.012.
(81) Agin, A., et al., Metabolomics – an overview. From basic principles to potential biomarkers (part 1)*, Médecine Nucléaire*, **2016***, 40,* 4–10. doi: 10.1016/j.mednuc.2015.12.006.
(82) Dufour-Rainfray, D., et al., Metabolomics – an overview. From basic principles to potential biomarkers (part 2)*, Médecine Nucléaire*, **2020***, 44,* 158–163. doi: 10.1016/j.mednuc.2020.02.004.
(83) Tan, S.Z.; Begley, P.; Mullard, G.; Hollywood, K.A.; Bishop, P.N., Introduction to metabolomics and its applications in ophthalmology*, Eye*, **2016***, 30,* 773–783. doi: 10.1038/eye.2016.37.
(84) Fiehn, O., Cellular Metabolomics: *The Quest for Pathway Structure,* Elsevier. Cambridge, MA, **2007**.
(85) Zhang, X.; Zhu, X.; Wang, C.; Zhang, H.; Cai, Z., Non-targeted and targeted metabolomics approaches to diagnosing lung cancer and predicting patient prognosis*, Oncotarget*, **2016***, 7,* 63437–63448. doi: 10.18632/oncotarget.11521.
(86) Rankin, N.J.; Preiss, D.; Welsh, P.; Sattar, N., Applying metabolomics to cardiometabolic intervention studies and trials: past experiences and a roadmap for the future*, International Journal of Epidemiology*, **2016***, 45,* 1351–1371. doi: 10.1093/ije/dyw271.
(87) Chen, Z.; Li, Z.; Li, H.; Jiang, Y., Metabolomics: a promising diagnostic and therapeutic implement for breast cancer*, OncoTargets and Therapy*, **2019***, 12,* 6797–6811. doi: 10.2147/OTT.S215628.
(88) Gonzalez-Covarrubias, V.; Martínez-Martínez, E.; Del Bosque-Plata, L., The Potential of Metabolomics in Biomedical Applications*, Metabolites*, **2022***, 12*. doi: 10.3390/metabo12020194.
(89) McMaster, M.C., *LC/MS: A practical user's guide,* Wiley. Hoboken, NJ, **2005**.
(90) Gey, M., *Instrumentelle Analytik und Bioanalytik: Biosubstanzen, Trennmethoden, Strukturanalytik, Applikationen,* Springer. Berlin, **2021**.

(91) Sanders, K.L.; Edwards, J.L., Nano-liquid chromatography-mass spectrometry and recent applications in omics investigations*, Analytical Methods*, **2020***, 12,* 4404–4417. doi: 10.1039/d0ay01194k.
(92) Hernández-Borges, J.; Aturki, Z.; Rocco, A.; Fanali, S., Recent applications in nanoliquid chromatography*, Journal of Separation Science*, **2007***, 30,* 1589–1610. doi: 10.1002/jssc.200700061.
(93) Alseekh, S., et al., Mass spectrometry-based metabolomics: a guide for annotation, quantification and best reporting practices*, Nature Methods*, **2021***, 18,* 747–756. doi: 10.1038/s41592-021-01197-1.
(94) Xiao, J.F.; Zhou, B.; Ressom, H.W., Metabolite identification and quantitation in LC-MS/MS-based metabolomics*, Trends in Analytical Chemistry*, **2012***, 32,* 1–14. doi: 10.1016/j.trac.2011.08.009.
(95) Gross, J.H.; Roepstorff, P., *Mass spectrometry: A textbook,* Springer. Berlin, **2011**.
(96) Matthiesen, R., *Mass spectrometry data analysis in proteomics,* Humana Press. Totowa, NJ, **2020**.
(97) Ridgeway, M.E.; Lubeck, M.; Jordens, J.; Mann, M.; Park, M.A., Trapped ion mobility spectrometry: A short review*, International Journal of Mass Spectrometry*, **2018***, 425,* 22–35. doi: 10.1016/j.ijms.2018.01.006.
(98) Kelstrup, C.D., et al., Rapid and deep proteomes by faster sequencing on a benchtop quadrupole ultra-high-field Orbitrap mass spectrometer*, Journal of Proteome Research*, **2014***, 13,* 6187–6195. doi: 10.1021/pr500985w.
(99) Scheltema, R.A., et al., The Q Exactive HF, a Benchtop mass spectrometer with a pre-filter, high-performance quadrupole and an ultra-high-field Orbitrap analyzer*, Molecular & Cellular Proteomics*, **2014***, 13,* 3698–3708. doi: 10.1074/mcp.M114.043489.
(100) Michalski, A., et al., Mass spectrometry-based proteomics using Q Exactive, a high-performance benchtop quadrupole Orbitrap mass spectrometer*, Molecular & Cellular Proteomics*, **2011***, 10,* M111.011015. doi: 10.1074/mcp.M111.011015.
(101) Meier, F., et al., Parallel Accumulation-Serial Fragmentation (PASEF): Multiplying Sequencing Speed and Sensitivity by Synchronized Scans in a Trapped Ion Mobility Device*, Journal of Proteome Research*, **2015***, 14,* 5378–5387. doi: 10.1021/acs.jproteome.5b00932.
(102) Bortel, P., Evaluation of phosphopeptide enrichment strategies for perturbation studies on in vitro systems employing ion mobility mass spectrometry. Master's thesis, *University of Vienna*, **2020**.
(103) Fernandez-Lima, F.A.; Kaplan, D.A.; Park, M.A., Note: Integration of trapped ion mobility spectrometry with mass spectrometry*, The Review of Scientific Instruments*, **2011***, 82,* 126106. doi: 10.1063/1.3665933.
(104) Meier, F., et al., Online Parallel Accumulation-Serial Fragmentation (PASEF) with a Novel Trapped Ion Mobility Mass Spectrometer*, Molecular & Cellular Proteomics***,** **2018***, 17,* 2534–2545. doi: 10.1074/mcp.TIR118.000900.
(105) Hochmeister, N., Charakterisierung von Cisplatin induzierten Apoptoseprozessen in Ovarialkarzinomzellen mittels Shotgun Proteomik. Bachelor's thesis, *University of Vienna*, **2020**.
(106) Ma, T., et al., Tetra-(p-tolyl)antimony(III)-Containing Heteropolytungstates, {(p-tolyl)SbIII}4(A-α-XW9O34)2n- (X = P, As, or Ge): Synthesis, Structure, and Study of Antibacterial and Antitumor Activity*, Inorganic Chemistry*, **2020***, 59,* 2978–2987. doi: 10.1021/acs.inorgchem.9b03322.

(107) Ritchie, M.E., et al., limma powers differential expression analyses for RNA-sequencing and microarray studies, *Nucleic Acids Research*, **2015**, *43,* e47. doi: 10.1093/nar/gkv007.
(108) Humphrey, S.J.; Karayel, O.; James, D.E.; Mann, M., High-throughput and high-sensitivity phosphoproteomics with the EasyPhos platform, *Nature Protocols*, **2018**, *13,* 1897–1916. doi: 10.1038/s41596-018-0014-9.
(109) Seiser, S., et al., Octenidine-based hydrogel shows anti-inflammatory and protease-inhibitory capacities in wounded human skin, *Scientific Reports*, **2021**, *11,* 32. doi: 10.1038/s41598-020-79378-9.
(110) Casado, P., et al., Kinase-substrate enrichment analysis provides insights into the heterogeneity of signaling pathway activation in leukemia cells, *Science Signaling*, **2013**, *6,* rs6. doi: 10.1126/scisignal.2003573.
(111) Horn, H., et al., KinomeXplorer: an integrated platform for kinome biology studies, *Nature Methods*, **2014**, *11,* 603–604. doi: 10.1038/nmeth.2968.
(112) Hornbeck, P.V., et al., PhosphoSitePlus, 2014: mutations, PTMs and recalibrations, *Nucleic Acids Research*, **2015**, *43,* D512-20. doi: 10.1093/nar/gku1267.
(113) Metz, K.S., et al., Coral: Clear and Customizable Visualization of Human Kinome Data, *Cell Systems*, **2018**, *7,* 347-350.e1. doi: 10.1016/j.cels.2018.07.001.
(114) Garcia-Calvo, M., et al., Inhibition of human caspases by peptide-based and macromolecular inhibitors, *The Journal of Biological Chemistry*, **1998**, *273,* 32608–32613. doi: 10.1074/jbc.273.49.32608.
(115) Wiernicki, B., et al., Cancer cells dying from ferroptosis impede dendritic cell-mediated anti-tumor immunity, *Nature Communications*, **2022**, *13,* 3676. doi: 10.1038/s41467-022-31218-2.
(116) Wong, D.L., et al., Epinephrine: a short- and long-term regulator of stress and development of illness: a potential new role for epinephrine in stress, *Cellular and Molecular Neurobiology*, **2012**, *32,* 737–748. doi: 10.1007/s10571-011-9768-0.
(117) Chobot, V.; Hadacek, F.; Weckwerth, W.; Kubicova, L., Iron chelation and redox chemistry of anthranilic acid and 3-hydroxyanthranilic acid: A comparison of two structurally related kynurenine pathway metabolites to obtain improved insights into their potential role in neurological disease development, *Journal of Organometallic Chemistry*, **2015**, *782,* 103–110. doi: 10.1016/j.jorganchem.2015.01.005.
(118) Shaw, A.A.; Wainschel, L.A.; Shetlar, M.D., The photochemistry of p-aminobenzoic acid, *Photochemistry and Photobiology*, **1992**, *55,* 647–656. doi: 10.1111/j.1751-1097.1992.tb08506.x.
(119) Tsuji, H.; Ogawa, T.; Bando, N.; Sasaoka, K., Purification and properties of 4-aminobenzoate hydroxylase, a new monooxygenase from Agaricus bisporus, *The Journal of Biological Chemistry*, **1986**, *261,* 13203–13209.
(120) Dasari, S.; Tchounwou, P.B., Cisplatin in cancer therapy: molecular mechanisms of action, *European Journal of Pharmacology*, **2014**, *740,* 364–378. doi: 10.1016/j.ejphar.2014.07.025.
(121) Peng, F., et al., Glycolysis gatekeeper PDK1 reprograms breast cancer stem cells under hypoxia, *Oncogene*, **2018**, *37,* 1062–1074. doi: 10.1038/onc.2017.368.
(122) Mossmann, D.; Park, S.; Hall, M.N., mTOR signalling and cellular metabolism are mutual determinants in cancer, *Nature Reviews Cancer*, **2018**, *18,* 744–757. doi: 10.1038/s41568-018-0074-8.

(123) White, P.J., et al., The BCKDH Kinase and Phosphatase Integrate BCAA and Lipid Metabolism via Regulation of ATP-Citrate Lyase*, Cell Metabolism*, **2018***, 27,* 1281-1293.e7. doi: 10.1016/j.cmet.2018.04.015.
(124) Lopez, J., et al., Src tyrosine kinase inhibits apoptosis through the Erk1/2- dependent degradation of the death accelerator Bik*, Cell Death & Differentiation*, **2012***, 19,* 1459–1469. doi: 10.1038/cdd.2012.21.
(125) Sánchez-Bailón, M.P., et al., Src kinases catalytic activity regulates proliferation, migration and invasiveness of MDA-MB-231 breast cancer cells*, Cellular Signalling*, **2012***, 24,* 1276–1286. doi: 10.1016/j.cellsig.2012.02.011.
(126) Salaun, P.; Rannou, Y.; Prigent, C., Cdk1, Plks, Auroras, and Neks: the mitotic bodyguards*, Advances in Experimental Medicine and Biology*, **2008***, 617,* 41–56. doi: 10.1007/978-0-387-69080-3_4.
(127) Zhang, H.-L., et al., PKC βII phosphorylates ACSL4 to amplify lipid peroxidation to induce ferroptosis*, Nature Cell Biology*, **2022***, 24,* 88–98. doi: 10.1038/s41556-021-00818-3.
(128) Zhu, T.; Tsuji, T.; Chen, C., Roles of PKC isoforms in the induction of apoptosis elicited by aberrant Ras*, Oncogene*, **2010***, 29,* 1050–1061. doi: 10.1038/ onc.2009.344.
(129) Yi, J.; Zhu, J.; Wu, J.; Thompson, C.B.; Jiang, X., Oncogenic activation of PI3K-AKT-mTOR signaling suppresses ferroptosis via SREBP-mediated lipogenesis*, Proceedings of the National Academy of Sciences of the United States of America*, **2020***, 117,* 31189–31197. doi: 10.1073/pnas.2017152117.
(130) Zhou, H.; Li, X.M.; Meinkoth, J.; Pittman, R.N., Akt regulates cell survival and apoptosis at a postmitochondrial level*, The Journal of Cell Biology*, **2000***, 151,* 483–494. doi: 10.1083/jcb.151.3.483.

List of figures

List of tables